

Key Points:

- The 3D cloud structure of a severe low-echo centroid (LEC) convection case is poorly simulated with three popular two-moment microphysics schemes
- Over-prediction of convective core heights and upper-level cloud fraction suggest deficiencies in the microphysics schemes in simulating LEC
- Simulated brightness temperature is most sensitive to cloud top height and vertical distribution of ice particles

Correspondence to:

K. Zhu and M. Xue,
zhukf@cma.gov.cn;
mxue@ou.edu

Citation:

Yang, N., Zhu, K., & Xue, M. (2022). Investigation of the convection-allowing prediction error of an extreme precipitation event of China using CRTM-simulated brightness temperature. *Journal of Geophysical Research: Atmospheres*, 127, e2022JD036760. <https://doi.org/10.1029/2022JD036760>

Received 11 MAR 2022

Accepted 10 SEP 2022

Investigation of the Convection-Allowing Prediction Error of an Extreme Precipitation Event of China Using CRTM-Simulated Brightness Temperature

Nan Yang¹ , Kefeng Zhu² , and Ming Xue^{1,3} 

¹Key Laboratory of Mesoscale Severe Weather/Ministry of Education and School of Atmospheric Sciences, Nanjing University, Nanjing, China, ²CMA Key Laboratory of Transportation Meteorology and Nanjing Joint Institute for Atmospheric Sciences, Nanjing, China, ³Center for Analysis and Prediction of Storms and School of Meteorology, University of Oklahoma, Norman, OK, USA

Abstract An extreme rainfall case occurred on 20 July 2016 in northern China, producing over 600 mm of maximum 24 hr accumulated rainfall. The case is characterized by low-echo centroid (LEC) based on radar observations. It is simulated by Weather Research and Forecasting model at 4 km grid spacing using the Morrison two-moment microphysics scheme. Infrared brightness temperature (BT) simulated using a radiative transfer model together with simulated reflectivity are used to evaluate the simulated cloud structures. In general, the model predicts the rainfall amount, location, and propagation well. However, it fails to accurately predict the three-dimensional cloud structures. The predicted convective cores (>35 dBZ) are higher than the freezing level, suggesting the presence of active cold-cloud processes while the observed LEC suggests that warm-cloud processes dominate. The simulation also produces too many upper level clouds and over-predicts the fractions of overshooting clouds, resulting great over-prediction of cloud top height (CTH). Additionally, the sensitivity of simulated BT to predicted cloud properties including CTH, cloud species and hydrometeor effective radii are examined to better understand the sources of error in simulated BT. Among those factors, CTH is found to be most critical to BT simulation. For every kilometer of CTH over-prediction, there is about 6.431 K of negative BT bias owing to the lapse rate and the absorption and scattering effects of cloud particles. For most cloudy regions, cloud ice dominates the effect on simulated BT. Using diagnosed effective radii of simulated hydrometeors within the radiative transfer model results in small improvement to the BT simulation.

1. Introduction

Clouds are essential part of precipitation systems. Latent heat released in clouds and the radiative effects of clouds can affect the thermodynamics and dynamics of the atmosphere, which in turn impact large-scale circulations (Karlsson, 1996). Cloud properties have a direct impact on how severe weather develops, including convective precipitation. It is critical to accurately predict the extent, structure, and evolution of clouds for forecasting convective weather. However, cloud-related processes are complex and have high nonlinearities, making convective clouds very difficult to predict. The major source of cloud observation is satellites. Satellite observations have been used to monitor the evolution of severe weather such as mesoscale convective systems (MCSs) (Mecikalski et al., 2010) and tropical cyclones (Xie et al., 2012). Satellite-derived products can be used for the prediction of convective initiation (Mecikalski & Bedka, 2006). Satellite data are also important for improving cloud and precipitation system forecasting.

In global numerical weather prediction (NWP) models, satellite observations have contributed most of the improvements in the last few decades through effective assimilation of the data over vast oceans (Collard & McNally, 2009). However, due to large errors and uncertainties of the simulated satellite radiances including infrared brightness temperature (BT) in cloudy regions in typical NWP models, the radiances assimilated in operational models are mostly limited to clear-sky radiances (Bauer, Ohning, et al., 2011; Geer et al., 2018). In some studies, the root-mean-square errors of the simulated BT in clouds are reported to reach as high as 20–40 K (Martin et al., 1994; Shi et al., 2018), making direct assimilation of BT observations difficult because direct assimilation tries to reduce errors in the forecast background by appropriately adjusting model state variables. The large mismatch between observed and simulated BTs can lead to erroneous adjustments that can produce more damage than benefit. Among other problems, the positional error of simulated clouds and unrealistic representation of cloud particles such as ice categorization, shape, and particle sizes (Bauer, Auligne, et al., 2011;

Bauer, Ohring, 2011; Otkin, 2010) within convection allowing or resolving models, as well as large uncertainties in hydrometeor forecast from microphysics scheme (Bauer, Ohring, et al., 2011), can all lead to large errors in the simulated radiance (Bauer, Auligne, et al., 2011; Bennartz & Greenwald, 2011; Weng, 2007). The assimilation of cloudy radiances remains inadequately exploited (Gustafsson et al., 2018; Qin et al., 2013; Zou & Da, 2014; Zou et al., 2011) and although some recent case-study-based efforts have shown somewhat encouraging results (Honda et al., 2018; Jones et al., 2020; Minamide & Zhang, 2018; Sawada et al., 2019; Zhang et al., 2018). To be able to better assimilate cloudy radiance data, it is important to investigate and understand the key sources of errors for simulated satellite radiances (Cintineo et al., 2014; Griffin et al., 2021).

Several recent studies have used satellite data to assess the accuracy of predicted clouds in NWP models. Otkin and Greenwald (2008) used satellite observations to assess the accuracy of different cloud microphysics and PBL schemes in the Weather Research and Forecasting (WRF) model (Skamarock et al., 2008) run at 4 km horizontal grid spacing. They found that differing assumptions made by microphysics schemes have a substantial impact on the simulation of cloud properties. Compared to single-moment microphysics schemes, double-moment schemes produced a broader cirrus shield and a relatively uniform cloud appearance, which was closer to observation. In contrast, single-moment schemes produced large, clear areas between the cumulus cells and underestimated the upper-level clouds, which may have been due to the different treatments of ice microphysical processes. Similar findings were reported by Jankov et al. (2011), who compared the performance of five single- and double-moment schemes in WRF. The relatively simple Purdue–Lin microphysics scheme was the least accurate. Large uncertainties remain in microphysical processes, especially ice-phase-related ones (Cintineo et al., 2014).

The above studies so far have focused mostly on deep convection systems (of the United States region), which are usually dominated by cold-rain processes. Warm-season heavy rainfalls also often produced by a type of low-echo centroid (LEC) systems, which is dominated by warm-rain processes. The LEC storm is defined as the storm whose cell centroid or highest reflectivity is located below the 0°C freezing level (Vitale & Ryan, 2013). The high precipitation efficiency of LEC systems often leads to catastrophic flash floods. Extreme rainfall events, including the Big Thompson storm (Maddox et al., 1978), the Rapid City storm (Caracena et al., 1979; Maddox et al., 1978), the Rapidan storm (Pontrelli et al., 1999; Smith et al., 1996), and the Fort Collins storm (Landel et al., 1999; Petersen et al., 1999) of the United States, and as well as several record-breaking extreme rainfall events in China (Huang et al., 2019; Zhong et al., 2015), were all caused by LEC storms. In this study, the performance of convection-allowing model (CAM) forecast using WRF for an extreme rainfall-producing LEC storm of northern China is evaluated by comparing radiative-transfer-model-simulated BT with observations of the Himawari-8 geostationary satellite while simulated radar reflectivity is also compared with operational radar observations. Special attention is paid to the sensitivity of simulated BT to cloud top height (CTH), and cloud hydrometeor content and distributions.

Bias or error in cloud properties produced by the forecast model is the most important source of error in simulated BT in cloudy regions. With the forecast model, different microphysical schemes tend to produce different cloud and hydrometeor profiles and distributions because of different treatments for certain processes. For example, the Morrison (Morrison et al., 2009) scheme allows for a maximum ice number concentration of 10 cm⁻³, which is much higher than the 0.25 cm⁻³ of the Thompson (Thompson et al., 2008) scheme (Cintineo et al., 2014). As a result, the former scheme may produce more upper-level ice particles than the latter. Tiwari et al. (2018) also showed that the Morrison scheme produced larger ice mixing ratios than other schemes, particularly above 400 hPa, while the Thompson scheme produces more snow content. The distribution of hydrometeor species will influence the predicted optical profiles in radiance transfer calculations, and significantly affect the simulated BT. The other source of error is with the representation of cloud optical properties within the radiative transfer model. Sieron et al. (2017, 2018) showed that incorrect representation of particle sizes in the Community Radiative Transfer Model (CRTM) (Han et al., 2006; Weng, 2007) look-up table is one of the error sources of simulated BT. Effective radius of certain hydrometeor species, which is associated with the particle size distribution of the species, is often set to a constant value in many early applications, presumably because single-moment microphysics schemes were used so that effective radius is not predicted. In this study, sensitivity of simulated BT to simulated cloud properties and as well as the effective radius will be investigated. Performance and deficiency of the two-moment Morrison microphysics schemes used are inferred because on the evaluations.

The rest of the paper is organized as follows. Section 2 describes the extreme rainfall case of northern China. Observed satellite data from the Advanced Himawari Imager (AHI) on board of the Himawari-8 satellite of Japan

Meteorological Agency as well as the WRF model configuration are also introduced. Section 3 presents the design of sensitivity experiments and the calculation of the CTH and effective radius. A traditional evaluation of the forecast performance and the verification results against Himawari-8 satellite radiance are presented in Section 4. The sensitivities of the simulated BTs to cloud properties are discussed in Section 5. A summary and conclusions are given in Section 6.

2. Extreme Rainfall Case, Numerical Simulation, and Satellite Observation

2.1. Overview of the Extreme Rainfall Case

From 19 to 21 July 2016, an extreme heavy rainfall event occurred in northern China. This long-lasting precipitation system produced new records of 24-hr accumulated rainfall at many rain gauge stations. The daily maximum rainfall exceeded 600 mm on July 19 (Fu et al., 2017). Figure 1 shows the synoptic systems during the developing and mature stages of the precipitation system. At 1200 UTC 19 July 2016, synoptic systems including a 500-hPa shortwave trough in the northwest, a low-level vortex ahead of the upper-tropospheric trough, and a northwest Pacific subtropical high in the east, which provided favorable conditions for heavy precipitation (Figure 1). Warm and moist air from South China Sea was transported to the rainfall region through a southwesterly low-level jet (Figure 1b). The 500-hPa trough developed into a cut-off low pressure system between 1800 UTC 19 July and 0000 UTC 20 July; meanwhile, the low-level vortex gradually intensified and moved northeast. The coupling between the upper-level shortwave trough and low-level vortex caused rapid intensification of the low pressure center (Zhao et al., 2018) (see red and blue contours in Figures 1c and 1e) and strengthened the transportation of water vapor from the Bohai Sea to Beijing and its adjacent area (Figures 1d and 1f). The whole system was an example of a so-called Huang-Huai cyclone, a type of extratropical cyclone in the Huang and Huai River basins of China. The system reached its mature stage at around 0000 UTC 20 July 2016, when the surface low pressure center reached 992.7 hPa, about triple the standard deviation lower than the average pressure (Fu et al., 2017). Due to the blocking effect of the subtropical high in the east and the Yanshan Mountains in the north, the Huang-Huai cyclone moved slowly. A sustained warm conveyor belt was established between the subtropical high and the Huang-Huai cyclone, which transported abundant warm and moist air from the South China Sea to northern China. Another main moist flow pathway was from the Bohai Sea, which was mainly driven by the Huang-Huai cyclone (Figures 1f and 1h). This westerly airflow rich in moisture greatly enhanced the precipitation. According to Luo et al. (2020), the relative humidity in northern China exceeded 70% due to moisture flow from the Bohai Sea and the South China Sea.

2.2. WRF Model Configuration

The Advanced Research version of the WRF model (Skamarock et al., 2008) is used to simulate the extreme rainfall case described above. The configuration of physics schemes follows the settings of the real-time 4-km WRF forecasting system run at Nanjing University (Zhu et al., 2018), including the Morrison two-moment microphysics scheme (Morrison et al., 2009), version 2 of the Asymmetric Convection Model (ACM2) PBL scheme (Pleim, 2007), the CAM shortwave/longwave radiation scheme (Collins et al., 2004), and the Pleim–Xiu land surface model (Pleim & Xiu, 2003). This configuration was chosen based on multiphysics sensitivity experiments for a previous heavy rainfall event in Beijing region, Northern China (Zhu & Xue, 2016). Here, slightly different from the real-time settings, we use NCEP FNL Operational Global Analysis data with a $1^\circ \times 1^\circ$ resolution at 6-hr intervals as the initial and boundary conditions. The real-time WRF model uses the NCEP operational GFS analysis and forecasts as initial and boundary conditions, respectively. The horizontal grid spacing is 4 km and the grid has $520 \times 700 \times 50$ grid points. The forecast is initialized at 0000 UTC 19 July 2016 and run through 0000 UTC 21 July, covering most of the life cycle of the precipitation system.

2.3. Observed Satellite Data

The main observations used for evaluation of model simulations is BT from the Himawari-8 AHI sensor. Geostationary satellite Himawari-8 was launched on 7 October 2014 and is located at 140.7°E . The AHI infrared imager instrument on board has 16 bands: 3 for visible (1–3), 3 for near-infrared (3–6), and 10 for infrared (7–16) radiance (Bessho et al., 2016). For the infrared bands, the AHI spatial resolution is 2 km at nadir, and the central wavelengths are 3.9–13.3 μm . These bands can be further divided into four categories: shortwave, water vapor, specific

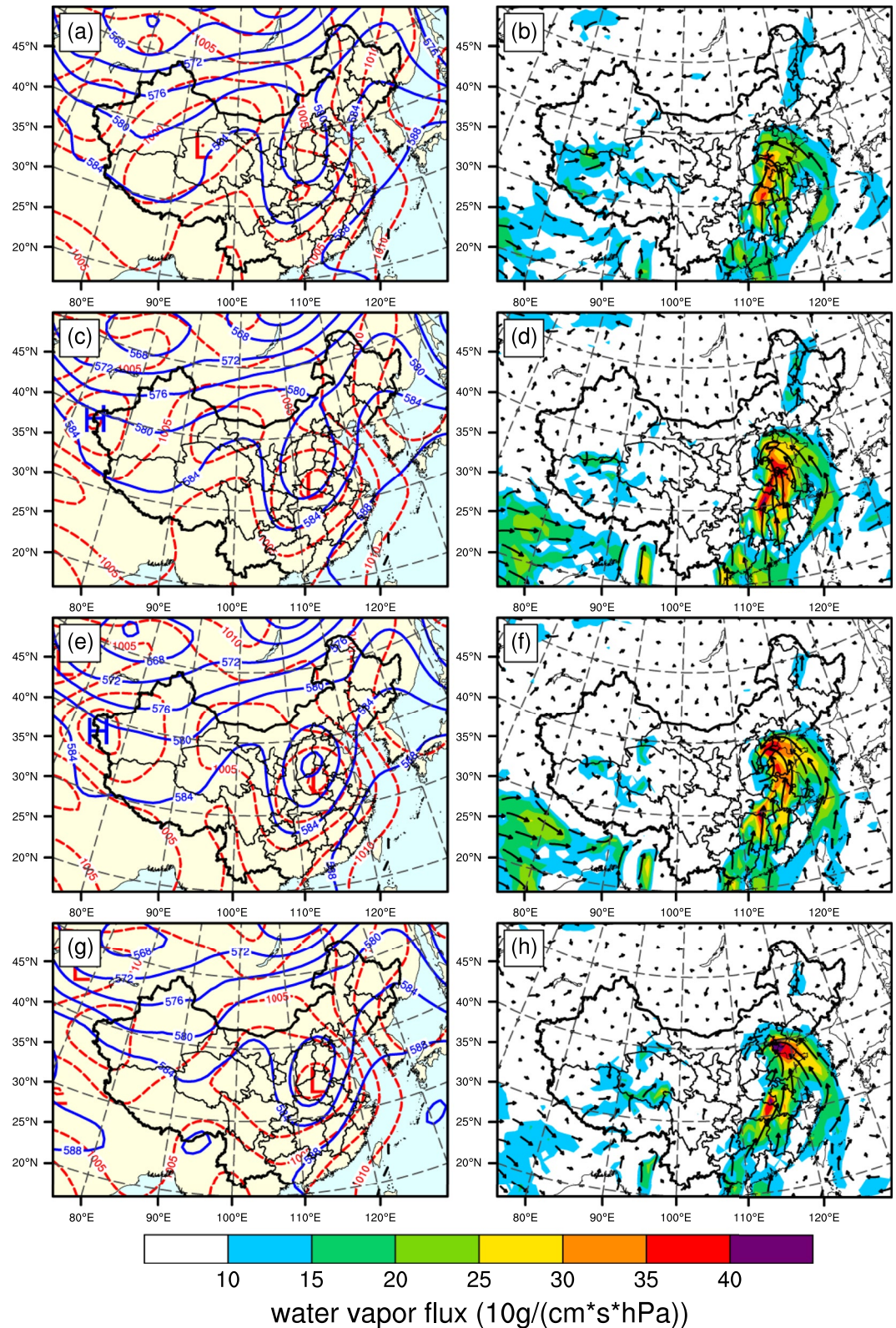


Figure 1. Panel(a) 500-hPa geopotential height (solid blue contours) and sea level pressure (dashed red contours). (b) Water vapor flux (color-shaded) and wind vectors at 925 hPa. Both (a) and (b) are for 1200 UTC 19 July 2016. The second to fourth rows are the same as the first row but for 1800 UTC 19 July 0000 UTC 20 July, and 0600 UTC 20 July of 2016, respectively. The data used in this figure are from the NCEP FNL $1^\circ \times 1^\circ$ analysis.

aerosol, and atmospheric window bands. The shortwave band (band 7: 3.9 μm) is used to monitor low-level clouds, fog, and other phenomena. The water vapor bands (bands 8–10: 6.2, 6.9, and 7.3 μm) are strongly affected by humidity in the middle-to-upper troposphere, and differences in sensitivity between them provide information on the vertical profile of humidity. The specific aerosol band (band 11: 8.6 μm) is sensitive to volcanic SO_2 gas while band 12 (9.6 μm) is the ozone absorption band. The atmospheric window bands (bands 13–15: 10.4, 11.2, and 12.4 μm) are sensitive to either cloud top properties or to the surface depending on whether or not clouds are present. Band 16 (13.3 μm) is the CO_2 absorption band, and is used for CTH assignment and thin cirrus opacity estimation. Here, we mainly use the 6.9- μm water vapor band and 10.4- μm atmospheric window band to evaluate our forecasts. The former peaks at 450 hPa while the latter peaks near surface. These two channels are also used to calculate the brightness temperature difference (BTD). Several studies have used BTD to evaluate cloud-height simulation in numerical models (Cintineo et al., 2014; Griffin et al., 2021; Mecikalski & Bedka, 2006). For both channels, the observed BTs are remapped to the WRF model grid.

3. Brightness Temperature Simulation and Cloud Properties

3.1. Simulation of BT and Sensitivity Experiments

The model version of AHI BTs is simulated using the CRTM (Han et al., 2010; Weng, 2007), from the vertical profiles of state variables and cloud hydrometeors predicted by WRF model. For cloudy grid points, the cloud type, mixing ratio profiles, and effective radii of hydrometeor variables are all needed. In CRTM, absorption and scattering properties are precalculated and stored in a look-up table based on Lorenz–Mie theory, using effective radius as the index. The optical properties are allocated to each hydrometeor species and their profiles in addition to the water content (from mixing ratio) profiles. From the bottom to the top of clouds, optical depth profiles and other scattering properties are calculated and used in radiance transfer calculations.

To understand the error sources of simulated BT, three groups of sensitivity tests are conducted. The first group is designed to assess the effect of forecast CTH error on BT simulation error. Satellite product of CTHs are compared with diagnosed CTHs from WRF output to assess forecast CTH error. Details will be stated in Section 3.2. The second group is designed to examine the contributions of individual hydrometeors using data denial method. For each experiment, we remove one type of hydrometeor, allowing the identification of the contribution to the simulated radiance from each hydrometeor type. The third group is designed to examine the impact of hydrometeor particle effective radii. In many radiance simulation software packages, the effective radius for each microphysical species is often set to constant, especially when a single-moment microphysics scheme is used (Cintineo et al., 2014). Constant effective radius is inconsistent with the assumptions made by multimoment microphysics parameterization schemes. With a double-moment scheme, the effective radii of hydrometeors can be diagnosed using the model predicted mixing ratios and total number concentrations, as will be discussed in detail in Section 3.3. BT simulation results using diagnosed and fixed effective radii will be compared.

3.2. Cloud Top Height

The infrared radiance obtained from geostationary satellites for a given location is markedly effected by clouds. This is because the height of their maximum sensitivity depends strongly on the presence and vertical location of clouds. In CRTM, there is no direct input of CTH, but it can be reflected by cloud/hydrometeor content profiles. Observed CTH can be obtained from the Himawari-8 cloud product, and for direct comparison, the predicted CTH is calculated as follows.

For the cloudy radiance computation, we need to first detect the clouds. The cloud detection algorithm of forecast cloud field is based on the relative humidity threshold method (Shi et al., 2018),

$$\text{cloudcover}_k = \begin{cases} 0, & \text{if } 950 < P_k \leq 1000\text{hPa}, \\ RH(k) \times 0.08 - 7.00, & \text{if } 700 < P_k \leq 950\text{hPa} \\ RH(k) \times 0.06 - 5.00, & \text{if } 450 < P_k \leq 700\text{hPa} \\ RH(k) \times 0.08 - 7.00, & \text{if } 100 < P_k \leq 450\text{hPa} \\ 1, & \text{if } RH(k) \geq 100 \\ 0, & \text{if } RH(k) \leq 0 \end{cases} \quad (1)$$

where the cloud cover of each pressure layer k is calculated through the relative humidity RH , in which $cloudcover = 0$ indicates no cloud and “1” indicates complete cloud cover. The pixels are classified as cloudy in the forecast when at least one layer is completely cloudy. For observation, the Himawari-8 level-2 cloud type products (Lai et al., 2019) are employed to classify cloudy and clear sky. In this study, to reduce the difference between the forecast and observation, we only compare the “hit” points. That is, the pixels are defined as cloudy (clear) pixels only when they are classified as cloudy (clear) in both the forecast and observation.

Observed CTH and cloud top temperature (CTT) are obtained from the level-2 CTH products of Himawari-8 (Min et al., 2017, 2020). The Cloud Height Algorithm (FCHA) utilizes two infrared window channels (11.0- μm , 12.0- μm) sensitive to cloud microphysics and a CO_2 absorption channel (13.3- μm) sensitive to CTH to calculate CTT. Loop over the temperature profile provided by the NWP and fast radiative transfer model used in the retrievals of cloud properties, CTH is obtained by interpolating height to the level of CTT. The uncertainty of satellite retrieved CTH should be noted since it depends on the profile of temperature from the model used in the retrieval process.

For the forecast, integrating the layer absorption coefficients (Dudhia, 1989) of cloud ice, cloud water, and water vapor along the path downwards from model top, cloud top is defined as the level of unit optical depth into the cloud. CTT and CTH are obtained by interpolating the temperature and height to the level of cloud top.

3.3. Effective Radius

In CRTM, cloud optical parameters are calculated with the general Mie theory using a modified gamma distribution function (Han et al., 2006). The specific absorption and scattering properties of the various hydrometeor species are contained in look-up tables, including frequency, effective radius, and, for liquid species, temperature as its input parameters (Sieron et al., 2017). Effective radius, as an input variable in the CRTM Cloud Absorption Scattering Model, determines the absorption and scattering properties of individual hydrometeor species, and thus affects the final calculated radiation and BT. For most applications of the Fast Radiative Transfer Model, the effective radii are set as constant values. Shahabadi et al. (2016) used three effective ice particle radii (10, 50, and 80 μm) and two effective liquid particle radii (10 and 13 μm , over land and sea). Cintineo et al. (2014) used effective radii of 20, 50, 1,000, 100, and 500 μm for cloud water, cloud ice, rain, snow, and graupel, respectively, for the simulation of GOES-R Advanced Baseline Imager BT when evaluating convection-allowing WRF realtime forecasts over the United States. For a hydrometeor species with a size distribution $N(D)$ where D is the diameter, the general formula for the effective radius r_e is (Hansen & Travis, 1974):

$$r_e = \frac{\int \pi D^3 N(D) dD}{2 \int \pi D^2 N(D) dD}. \quad (2)$$

Effective radius represents the “mean” size of hydrometeor particles and directly affect the radiative properties of the particles, and is therefore conceptualized as the “mean radius for scattering.” The cloud droplet effective radius is proportional to the volume of spherical droplets over a projected area. Assuming that scattering occurs on the drop surface (D^2), and absorption occurs inside the drop volume (D^3), the net reflectance is related to the ratio of scattering and absorption, which is r_e^{-1} .

Following Thompson et al. (2016), cloud particle assumptions in the microphysics scheme are used to calculate the effective radius. For Morrison two-moment microphysics scheme, the cloud and precipitation particle size distributions are represented by gamma functions (Morrison et al., 2009):

$$N_x(D) = \frac{N_{Tx} \lambda_x^{\alpha_x+1}}{\Gamma(\alpha_x+1)} D^{\alpha_x} e^{-\lambda_x D}, \quad (3)$$

where $N_x(D)$ is the total number concentration per unit volume of particles of diameter D for hydrometeor variable x , N_{Tx} is the total number concentration, λ_x is the slope parameter, α_x is the shape parameter, and Γ is the Euler gamma function.

Equation 3 can be integrated analytically over all sizes. Specifically, the p th moment of the distribution, $M_x(p)$, is given by

$$M_x(p) = \int_0^{\infty} D_x^p N(D_x) dD_x = \frac{N_{Tx}}{\lambda_x^p} \frac{\Gamma(1 + \alpha_x + p)}{\Gamma(1 + \alpha_x)}. \quad (4)$$

Particle mass in a hydrometeor category is related to its diameter D_x by

$$m_x(D_x) = c_x D_x^{d_x}, \quad (5)$$

with $d_x = 3$ and $c_x = \frac{\pi}{6} \rho_x$ for spheres. The water content is then calculated as follows:

$$Q_x = \rho q_x = \int m_x(D_x) N(D_x) dD_x = \frac{\pi}{6} \rho_x M_x(3), \quad (6)$$

where ρ is the density of air. For spheres, $p = d_x = 3$, we get

$$\lambda_x = \left[\frac{\pi \rho_x \Gamma(1 + \alpha_x + 3) N_{Tx}}{6 \Gamma(1 + \alpha_x) \rho q_x} \right]^{1/3}. \quad (7)$$

Effective radius r_e can be derived from Equations 2 and 4 and is of the form

$$r_{ex} = \frac{1}{2} \frac{M_x(3)}{M_x(2)} = \frac{1}{2} \frac{\Gamma(1 + \alpha_x + 3)}{\lambda_x \Gamma(1 + \alpha_x + 2)}. \quad (8)$$

For cloud droplets, the predicted droplet number concentration is fixed ($N_{Tc} [m^{-3}] = 250 * 10^6$), and α_c is calculated as a function of the predicted droplet number concentration following the observations of Martin et al. (1994):

$$\alpha_c(N_{Tc}, P, T) = \frac{1}{pgam^2} - 1 \in [2, 10], \quad (9)$$

where

$$pgam = 0.0005714 * \frac{P * N_{Tc}}{287.15 * T * \rho} + 0.2714, \quad (10)$$

in which P is the atmospheric pressure (Pa) and T is the temperature (K).

For precipitation species (rain, snow, graupel) as well as cloud ice, a simplified inverse exponential function, or Marshall–Palmer distribution, is adopted with $\alpha_x = 0$. Equation 8 can then be reduced to a one-parameter function,

$$r_{ex} = \frac{3}{2\lambda_x}, \quad (11)$$

where

$$\lambda_x = \left[\frac{\pi \rho_x N_{Tx}}{\rho q_x} \right]^{1/3}. \quad (12)$$

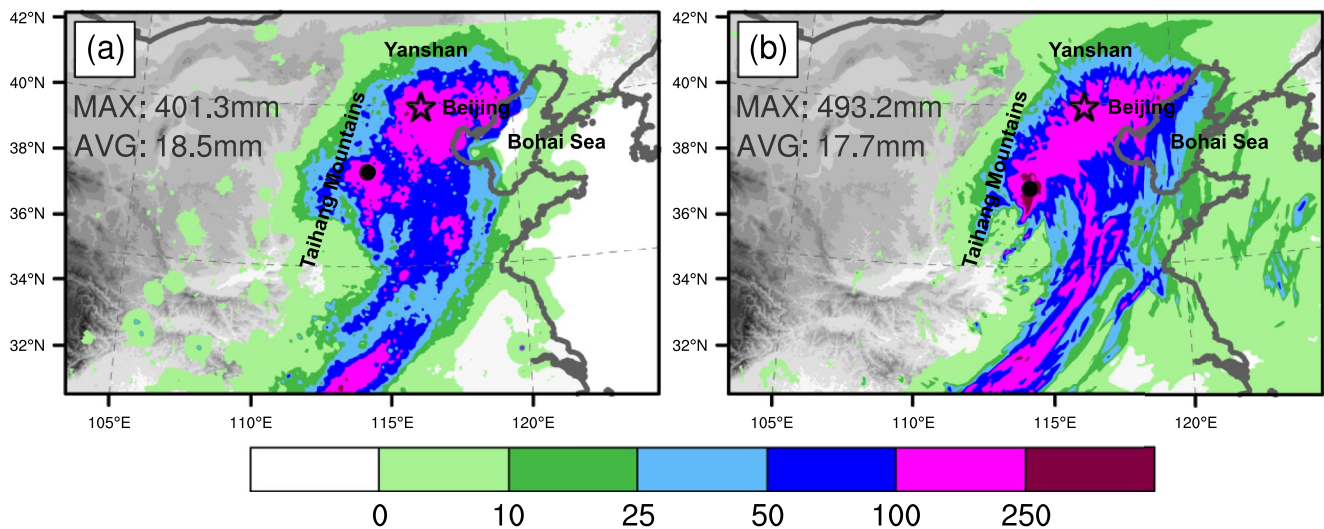


Figure 2. The 24-hr accumulated rainfall between 1200 UTC 19 July and 1200 UTC 20 July 2016 for the (a) observation and (b) forecast. The values of daily maximum and average rainfall are shown in the picture, with black dots indicating the locations of maximum rainfall. The observed precipitation data are from the $0.05^\circ \times 0.05^\circ$ merged precipitation analysis product (over $70^\circ\text{--}140^\circ\text{E}$, $15^\circ\text{--}60^\circ\text{N}$) produced by the China Meteorological Administration (CMA). Gray shading represents the terrain height. Beijing is marked with a black star.

The above formulations are used to calculate effective radii for cloud and hydrometeor species and passed to CRTM for calculating BT from WRF model output.

4. Overall Evaluation of the WRF Forecast

4.1. Evaluation of Forecast Precipitation Distribution and Reflectivity Structure

Figure 2 shows the observed and forecast 24-hr accumulated rainfall between 1200 UTC of 19 and 20 July 2016 for the extreme rainfall case. There are two observed rainfall maximum centers: one at the east foot of the Taihang Mountains and the other at the south foot of the Yanshan Mountains. The forecast reasonably reproduced these two centers though they appear more connected than in observation. The overall patterns of heavy precipitation are also similar. Compared to the observation, the forecast over-predicts the maximum amount somewhat (493.2 vs. 401.3 mm). The predicted domain-average rainfall amount is very close to observed though, being 17.7 versus 18.5 mm in the observation and forecast, respectively. Figure 3 shows the observed and forecast hourly accumulated rainfall at 6 hr intervals. During the developing stage of the precipitation system (before 0000 UTC 20 July 2016), the observed precipitation formed ahead of the upper level shortwave trough and a comma-shaped south–north-oriented main rain band was located in the eastern foothills of the Taihang Mountains (Figures 3a and 3c). The precipitation moved north as the Huang-Huai cyclone reached its mature stage. Due to the blocking effect of the subtropical high on the east side, the ridge of high pressure near the Sea of Japan, and the blocking effect of the Yanshan Mountains, the Huang-Huai cyclone moved very slowly. During that time, the precipitation was mainly located in the northeast of the Huang-Huai cyclone, and a long west–east rain band persisted along the south side of the Yanshan Mountains. Although convection was not as strong as that of the developing stage, it produced continuous heavy precipitation in Beijing and nearby areas (Figures 3e and 3g). Throughout the entire period, the forecast reproduces the spatial distribution and movement of precipitation in each stage well (Figures 3b–3f and 3h). The intensity and location of the heavy precipitation centers are also in general agreement with the observation. Overall, the WRF forecast can be considered successful for this extreme rainfall event.

Figure 4 shows the radar observed and predicted composite reflectivity. We chose two times, 1200 UTC 19 July and 0000 UTC 20 July 2016, to represent the developing and mature stages of this rainfall event, respectively. The forecast depicts more intense embedded convective cores within the major rain band than observed. The reflectivity structure and evolution are more accurately reproduced. The vertical composite reflectivity, calculated as the maximum reflectivity across the 10 vertical slices indicated in Figure 4, are shown in Figure 5 for both observations and forecasts. The observed convective cores (>35 dBZ) reveal a “bottom heavy” structure throughout the

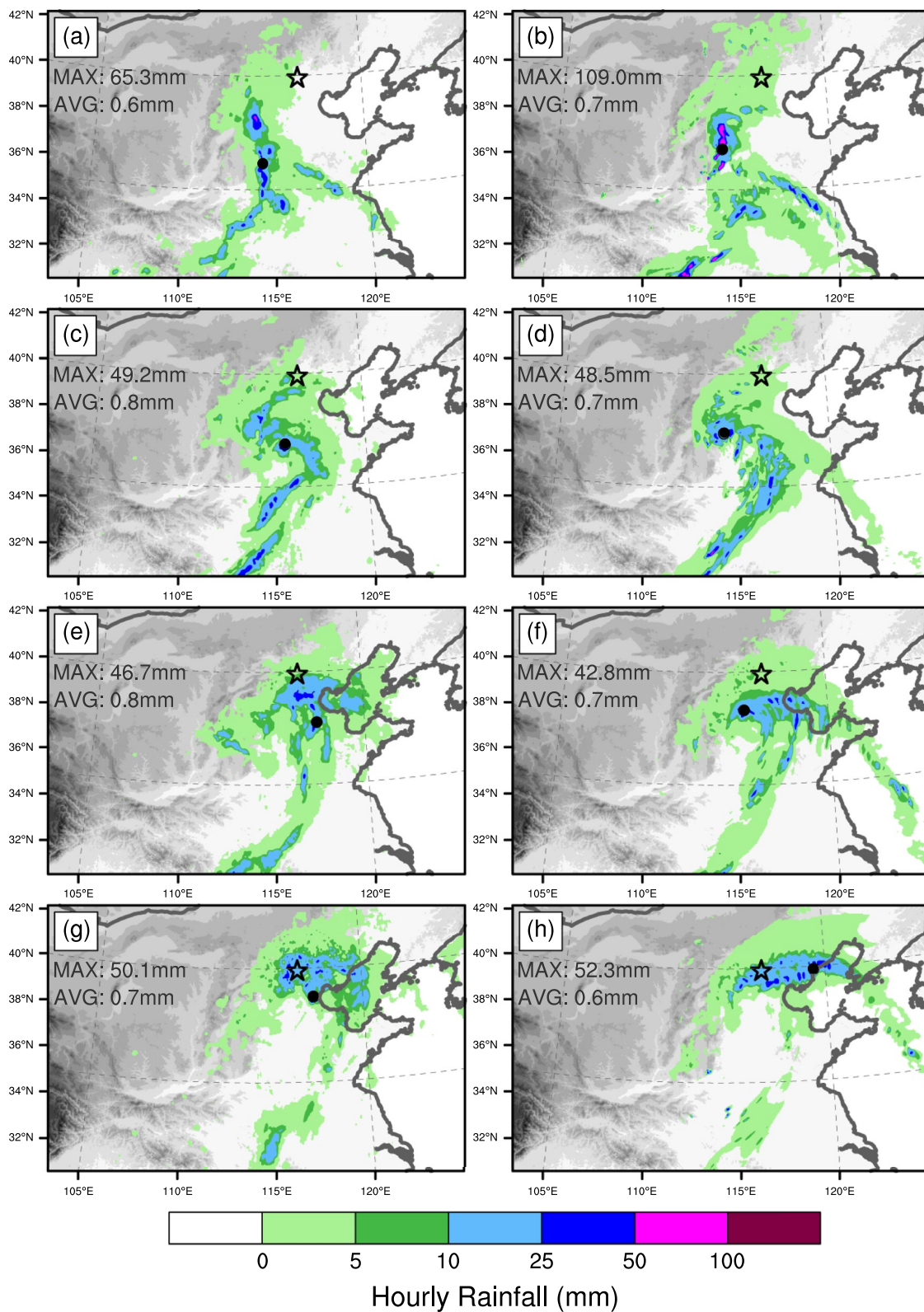


Figure 3. Hourly rainfall for the observation (left) and forecast (right): (a, b) 1200 UTC 19 July 2016; (c, d) 1800 UTC 19 July 2016; (e, f) 0000 UTC 20 July 2016; (g, h) 0600 UTC 20 July 2016.

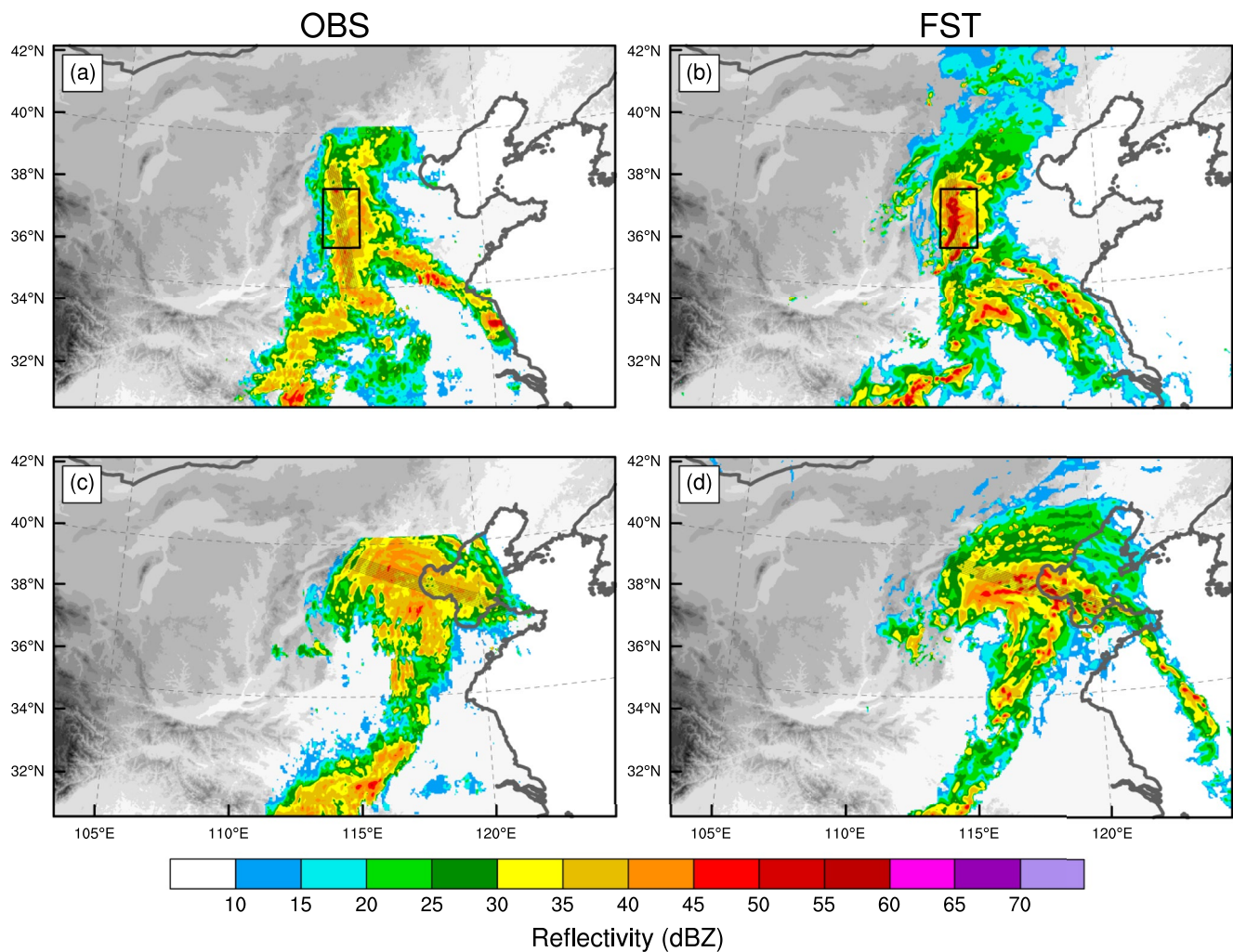


Figure 4. Composite reflectivity of the (a, c) observation and (b, d) forecast (control experiment) at (a, b) 1200 UTC 19 July 2016 and (c, d) 0000 UTC 20 July 2016. The black sharped rectangle area indicate the locations of 10 slices used for the calculation of vertical composite reflectivity in Figure 5. The black box represents the region used for the calculation of mean vertical profiles in Figure 7.

period. The highest reflectivity is seen below -10°C and is less than 60 dBZ. These observations suggest that the extreme event is a LEC storm, with warm-rain processes dominating (Vitale & Ryan, 2013).

The predicted convective cores, on the other hand, are clearly higher than observed. During the developing stage, the maximum height of the convective cores is above the -40°C line, and the peak reflectivity exceeds 60 dBZ, indicating that cold-cloud processes are also quite active and have contributed to or interacted with the processes of collision-coalescence. In the mature stage, although the predicted intensity is not as high as the developing stage, the maximum height of the convective cores in some locations is above -10°C , indicating that cold-cloud processes are also active for the production of precipitation within the model. The over-prediction of convective core height is not unique to the Morrison microphysics scheme. We rerun the case with Thompson aerosol-aware (Thompson & Eidhammer, 2014) and Milbrandt-Yau (Milbrandt & Yau, 2005) two-moment microphysics schemes and show the vertical cross sections at 1200 UTC 19 July 2016, corresponding to those in the top panels of Figure 5. It can be seen that the 30 dBZ echo reaches 14 km in Thompson simulation (Figure 6a) while a 45 dBZ convective core reaches 12 km in Milbrandt-Yau simulation (Figure 6b), all far exceeding those observed (Figure 5a). Therefore, the over-prediction problem appears to be common to microphysics schemes although the extent of over-prediction varies somewhat across the schemes.

To investigate possible microphysics errors causing the over-prediction, we show in Figure 7 the mean profiles of ice and liquid phase mixing ratios as well as observed and forecast reflectivity in precipitation region. As

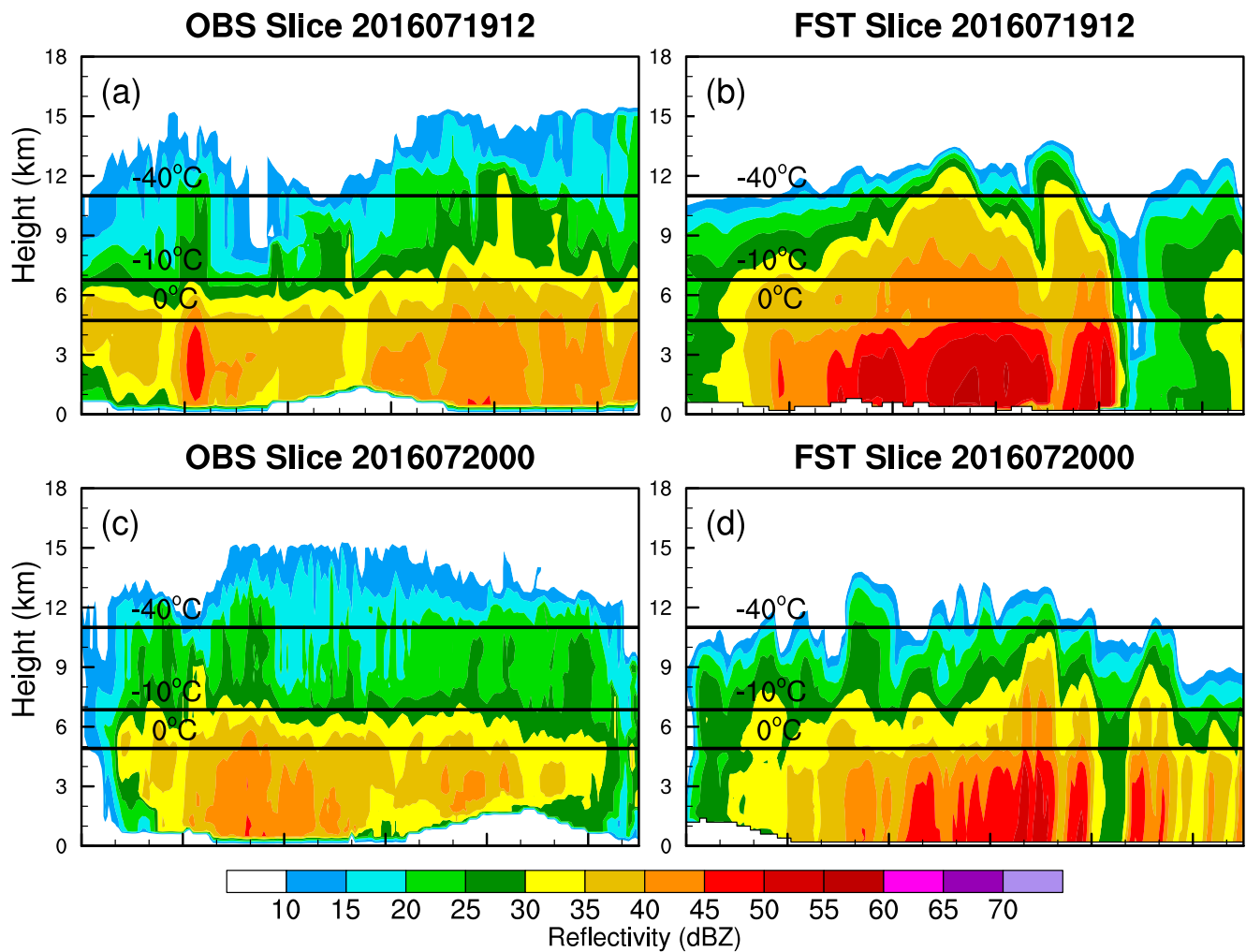


Figure 5. Vertical composite reflectivity of the (a, c) observation and (b, d) forecast at (a, b) 1200 UTC 19 July 2016 and (c, d) 0000 UTC 20 July 2016. The composite reflectivity is the maximum reflectivity across the 10 slices shown in Figure 4 (see thin lines). The black lines indicated the 0°C, −10°C, and −40°C levels, respectively.

discussed earlier, the synoptic environment was favorable for the development of heavy precipitation. In the forecast, the cold- and warm-cloud processes are activated almost simultaneously, and it can be seen that the ice and liquid contents appear concurrently (Figures 7c and 7d). The ice content then continues to grow and reaches its maximum between 9 and 12 hr of forecast. The latent heat released by the cold-cloud processes increases the ascending motion, which in turn intensifies the cold-cloud processes, resulting a typical deep convective structure (Figure 7c). Clearly, the forecast of Morrison scheme is dominated by both cold- and warm-cloud processes, which is not consistent with the observed LEC structure that should be dominated by warm-cloud processes (Vitale & Ryan, 2013). As we saw, the height of the observed reflectivity core does not show significant change, and the average reflectivity values larger than 35 dBZ are mostly below 0°C. By comparison, the forecast shows clear growth for the height of reflectivity core between the 9 and 16 hr of forecasts, and the average reflectivity larger than 35 dBZ reaches −10°C (Figures 7a and 7b). That means the convection of forecast is getting stronger, cloud-cloud processes play an important role on the precipitation. Apart from microphysics errors, too strong large-scale forcing can also cause over-prediction of convective core height. Large-scale forcing error is, however, hard to quantify.

4.2. Evaluation of Cloud Simulation Using Satellite Radiance

In this subsection, the prediction of cloud structure is evaluated using satellite infrared BT observations. Figure 8 compares the observed and simulated BTs of the 10.4-μm channel. In general, the overall simulated cloud patterns

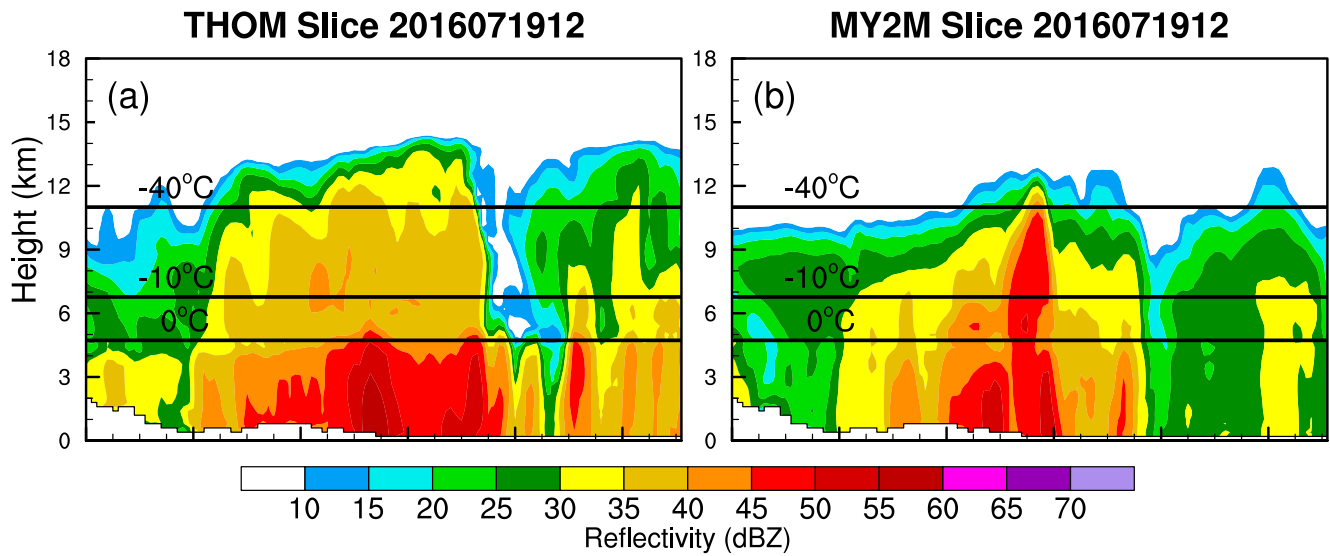


Figure 6. Vertical composite reflectivity of the forecasts of Thompson aerosol-aware and Milbrandt-Yau two-moment scheme at 1200 UTC 19 July 2016. The black lines indicated the 0°C, −10°C, and −40°C levels, respectively.

are quite similar to the observation throughout the simulation period although the simulated BT contains more small-scale details. The main difference is in the fraction of high-level clouds; the area of simulated high-level clouds (<220 K) is clearly larger than observed. Another clear difference is in the heavy-rain area (red contours). Specifically, the observed high-level clouds are mostly located in the anvil of the precipitation-producing MCS (Figures 8a and 8c), while the simulated radiance shows high-level clouds (<220 K) over the heavy-rain area of the MCS (Figures 8b and 8d). Here, we also examined two other microphysics schemes mentioned above, and found similar performance. The cloud top in the predicted heavy-rainfall area is higher than that in the observations, which is consistent with the above evaluation of reflectivity. Compared to the observations, the predicted maximum elevation of convective cores (enclosed by the 35 dBZ contour lines) are also higher (see Figures 5 and 6).

Figure 9 presents the difference in the vertical probability distribution between the observed and simulated radiance, which is calculated using a window (10.4 μm) and water vapor (6.9 μm) band. Similar plots were examined in Cintineo et al. (2014). In general, both channels show that the frequencies of BT between 200 and 230 K are over-predicted. This suggests that the Morrison microphysics scheme produces too many cold pixels throughout the forecast period. The differences for colder BT in the upper levels are mainly due to differences in cloud cover, and the over-prediction of cold pixels indicates that the forecast produces either too many high clouds or the simulated convection is too deep. For the 10.4- μm window band, the forecast underestimates the frequency of BT between 260 and 280 K, but over-predicts it between 290 and 300 K for most of the period. Those differences reveal that the forecast either underestimates the surface temperature or produces more low clouds. For the 6.9- μm water vapor band, there are too many grid points between 250 and 265 K, but too few points between 230 and 250 K. Cintineo et al. (2014) also found similar biases in the mid-to-upper troposphere for the Morrison and three other microphysics schemes. Comparison between sounding observations and WRF initial conditions suggested that those forecast biases in the mid-to-upper level were unrelated to the microphysics schemes, but instead were related to the bias in the water vapor content in the initial conditions that persisted during the forecast (Coniglio et al., 2013).

Two-dimensional histograms of 6.9–10.4- μm BTD versus 10.4- μm BT are shown in Figure 10. The BTD can be used to examine the performance of NWP models in the forecast of cloud height during the forecast period (Mecikalski & Bedka, 2006). Under clear-sky conditions, radiance emitted at 6.9 μm by the surface or low clouds is absorbed by water vapor in the lower troposphere. Most of the radiance at 6.9 μm is emitted by atmospheric water vapor between 200 and 500 hPa and peaks at 450 hPa. On the other hand, in the 10.4- μm band, absorption by atmospheric gases is weak, and thus the radiance at 10.4 μm mainly comes from the surface. In cloudy conditions, clouds absorb and scatter radiance from below. Radiance in both bands is emitted by the cloud

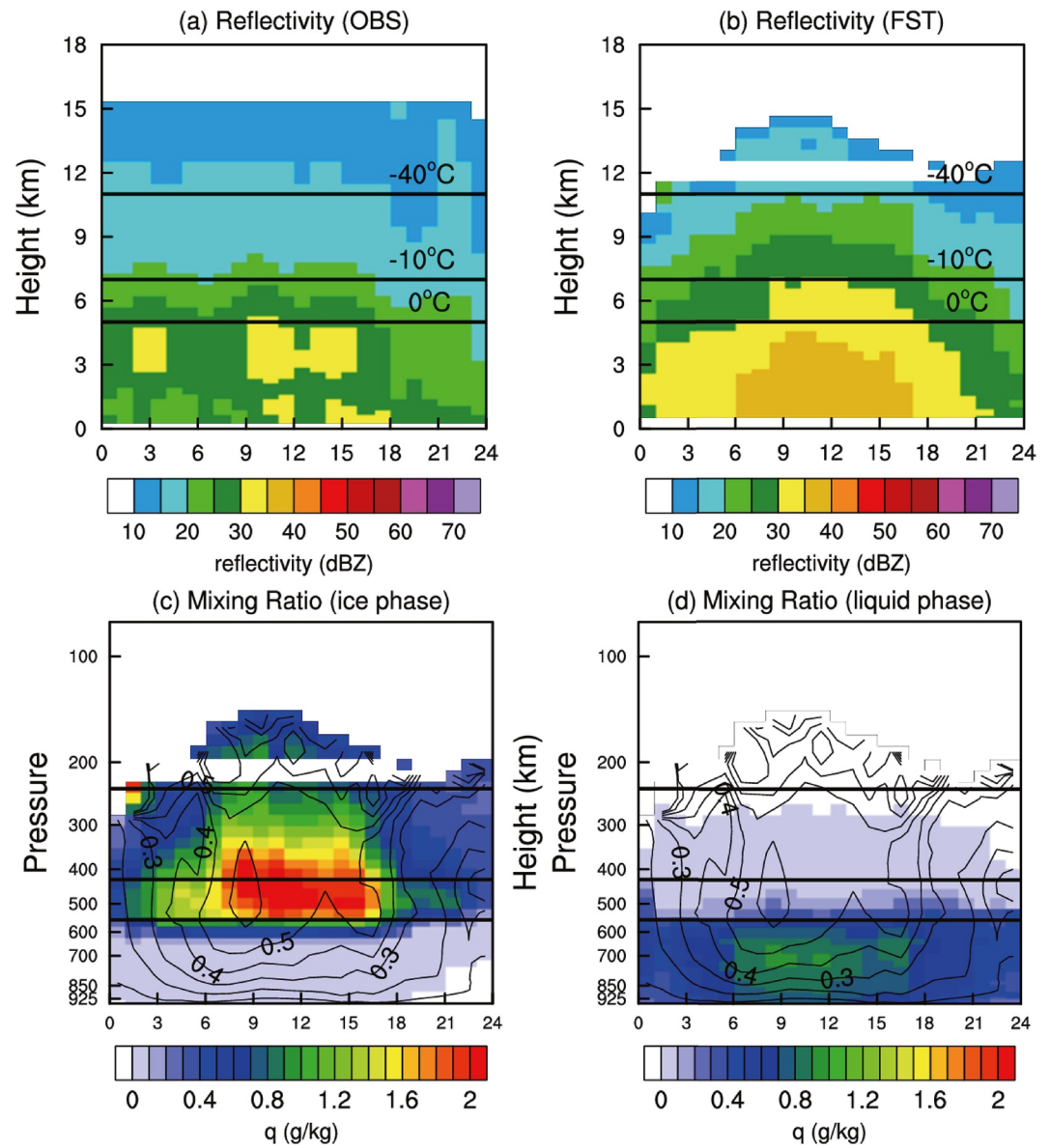


Figure 7. Mean vertical profile of (a) observed reflectivity, (b) forecast reflectivity, (c) mixing ratio of ice-phase particles, and (d) mixing ratio of liquid-phase particles for the precipitation region in Figure 4 (black box, >10 dBZ) from 0000 UTC 19 July to 0000 UTC 20 July (stage 1). The black thin lines in (c) and (d) are contours of the vertical velocity. The black thick lines in figures represent 0°C, -10°C and -40°C, respectively.

top. Because of the general decrease in temperature with height in the troposphere, BTD is mostly negative, with the largest differences occurring in clear-sky regions. Its value can represent the cloud height compared to the tropopause (Mecikalski & Bedka, 2006). The BTD thresholds used here for rough estimation of cloud height follow previous studies (Mecikalski & Bedka, 2006; Skamarock, 2004): from -30 to -10 K for low-to mid-level cloud tops (about 850–500 hPa); greater than -10 K for upper-level cloud tops; and greater than -2 K for overshooting tops (Cintineo et al., 2014). In general, the histogram shape of the forecast matches fairly well that of observation. The main difference is in the upper-left corner, where the BTD value and frequency of the forecast are both higher than observed. For BTD values above -2 K and BT less than 220 K (red box in Figure 9), the forecast shows more overshooting convection. For BTD values between -10 and -2 K, corresponding to the upper-level cloud tops in the troposphere, the forecast high-frequency pixels have larger BTD values with the same BT. This means the forecast not only produces too many upper-level clouds, but also over-predicts the cloud height.

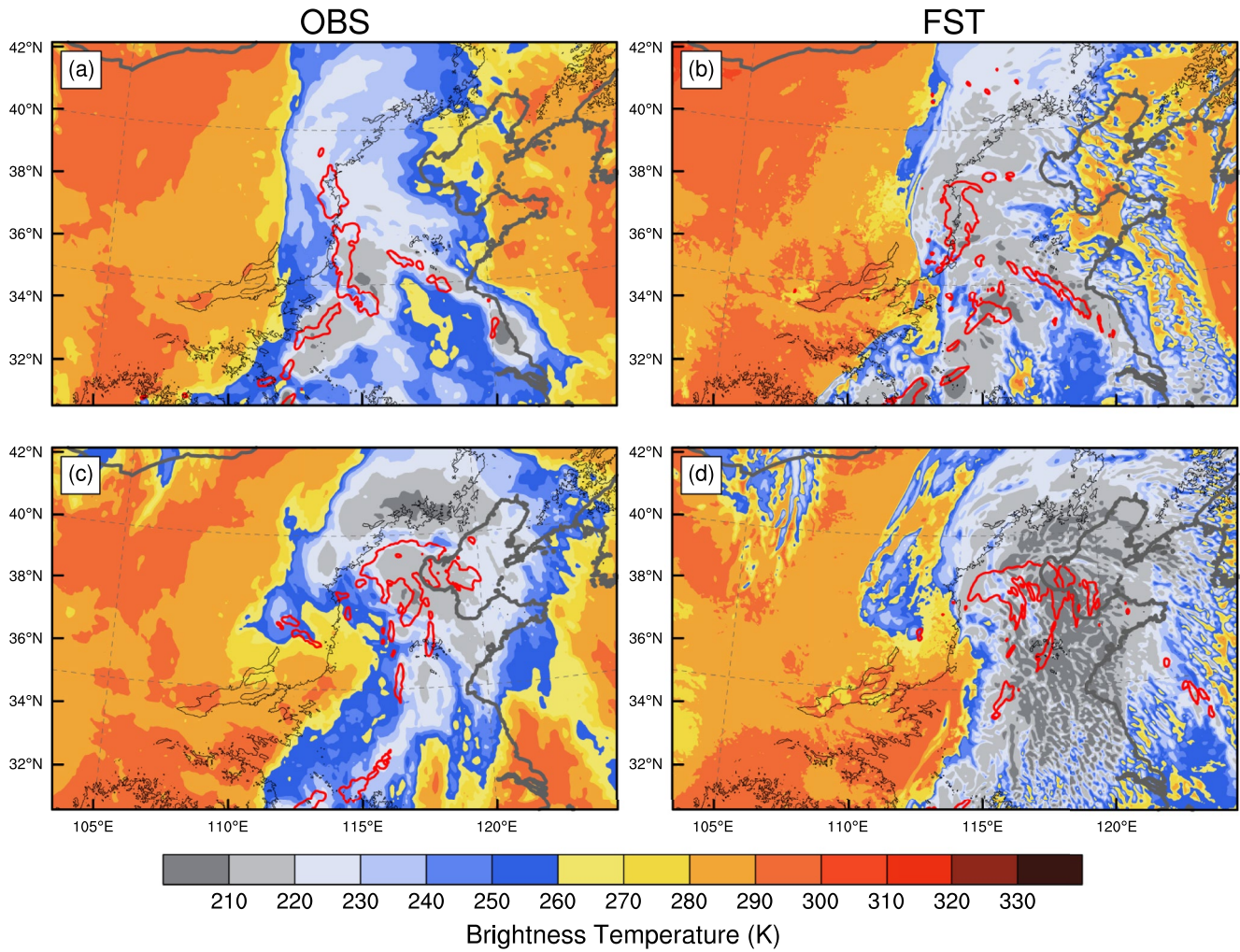


Figure 8. BT for the 10.4- μm window band of the (a, c) observation and (b, d) forecast at (a, b) 1200 UTC 19 July 2016 and (c, d) 0000 UTC 20 July 2016. The red line is the 10 mm hr^{-1} rainfall contour. The thin black line is the 500 m terrain height contour.

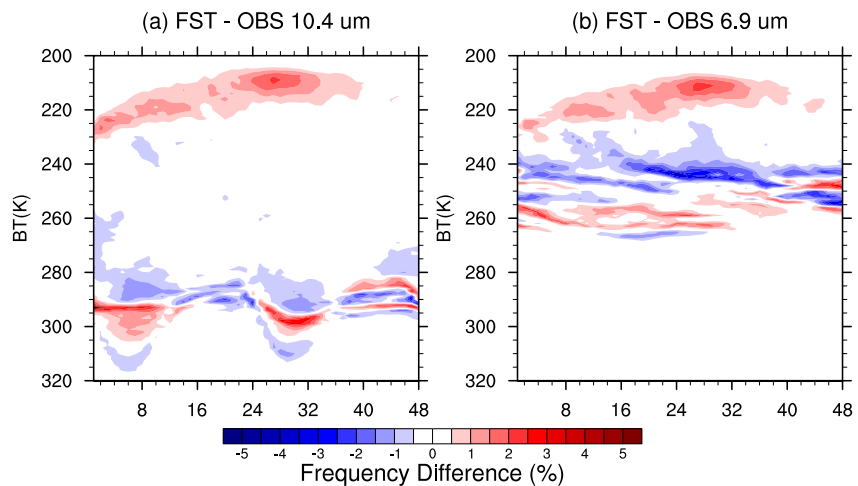


Figure 9. Distribution of BT frequency differences between forecasts and observations of the (a) 10.4- μm and (b) 6.9- μm IR channels. The x -axis is the forecast hours and the y -axis is the BT. A higher BT value indicates the point is closer to the surface, while a lower value means the point is in the upper level.

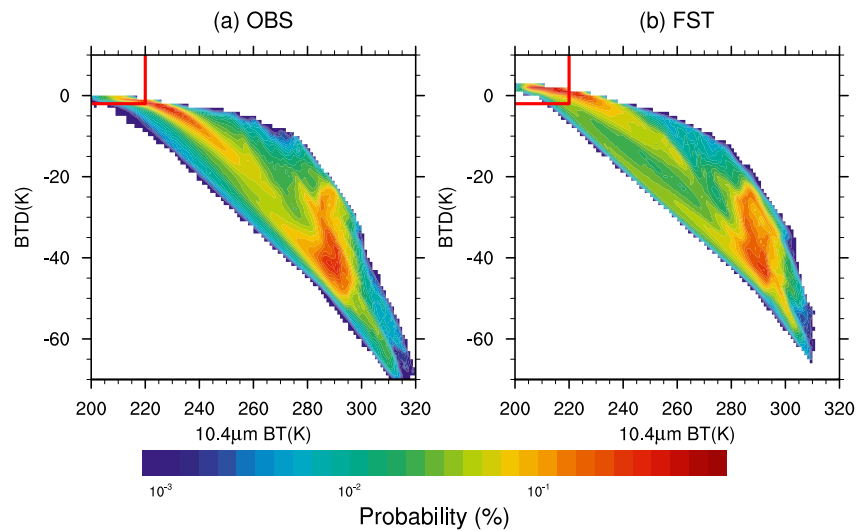


Figure 10. Two-dimensional histogram of the 6.9–10.4- μm BT D versus the 10.4- μm brightness temperature (time-averaged between the 7th and 48th forecast hours).

Fewer pixels are shown in the forecast result for BT D from -30 to -10 K. This indicates the forecast underestimates the mid-to upper-level clouds. In the lower right, the forecast lacks points where BT D is less than -65 K and BT is larger than 310 K, which is the result of the cold bias in the temperature forecast at the surface. The results of the BT D histograms are consistent with the previous analysis of Figure 9. Overall, for this LEC storm, the forecast not only produces too many high clouds, but also over-predicts the CTH of convection. Also, the forecast tends to underestimate the mid-to upper-level clouds but over-predict low clouds near the surface. The overshooting issue is more serious when compared to. These findings are very similar to those of Cintineo et al. (2014). A small difference is that the overshooting issue is more serious here, suggesting too active cold-processes for the simulated LEC storm in our case.

5. Sensitivity of Simulated BT to Cloud Properties

As shown in the above section, the forecast greatly underestimates the BT in the convection region of our LEC storm. Cloud properties such as CTH, hydrometer species, and their effective radii have a direct impact on the accuracy of the CRTM-simulated radiance. To identify the contribution of each factor, in this section, the sensitivity of the simulated BT bias to cloud properties is investigated.

5.1. Sensitivity of Simulated BT to CTH

For the cloudy area, the differences between the observed and simulated radiance are strongly linked to the difference in CTH. This is because the BT is heavily influenced by the CTT if the channel's weight function peak is below the cloud top. Figure 11 shows the observed and forecast CTH. The forecast reproduces the general pattern of the cloudy area very well (see CTH > 2 km). Consistent with the previous analysis, the CTH is clearly over-predicted, especially for the deep convection area. For both developing and mature stages, the forecast region of CTH above 12 km is clearly larger than that of observation. Figure 12 presents the time series of the mean CTH for BT D > -10 K (corresponding to high clouds in the troposphere). Except for the spin-up time for the first few forecast hours, the predicted CTH (red line) is consistently higher than that of the observation (black line) during the forecast period.

These biases of simulated CTH are the main factors behind the cold biases of the simulated radiance for our LEC storm. The correlation between the bias of the simulated CTT and CTH is calculated, and the results are presented in Figure 13. It can be seen that the biases of the simulated CTT have a significant linear relationship with the biases of the simulated CTH. For high clouds and overshooting tops (BT D > -10 K), every 1 km of over-prediction in the CTH can lead to a -5.984 K underestimation of the CTT (Figure 13a). These biases

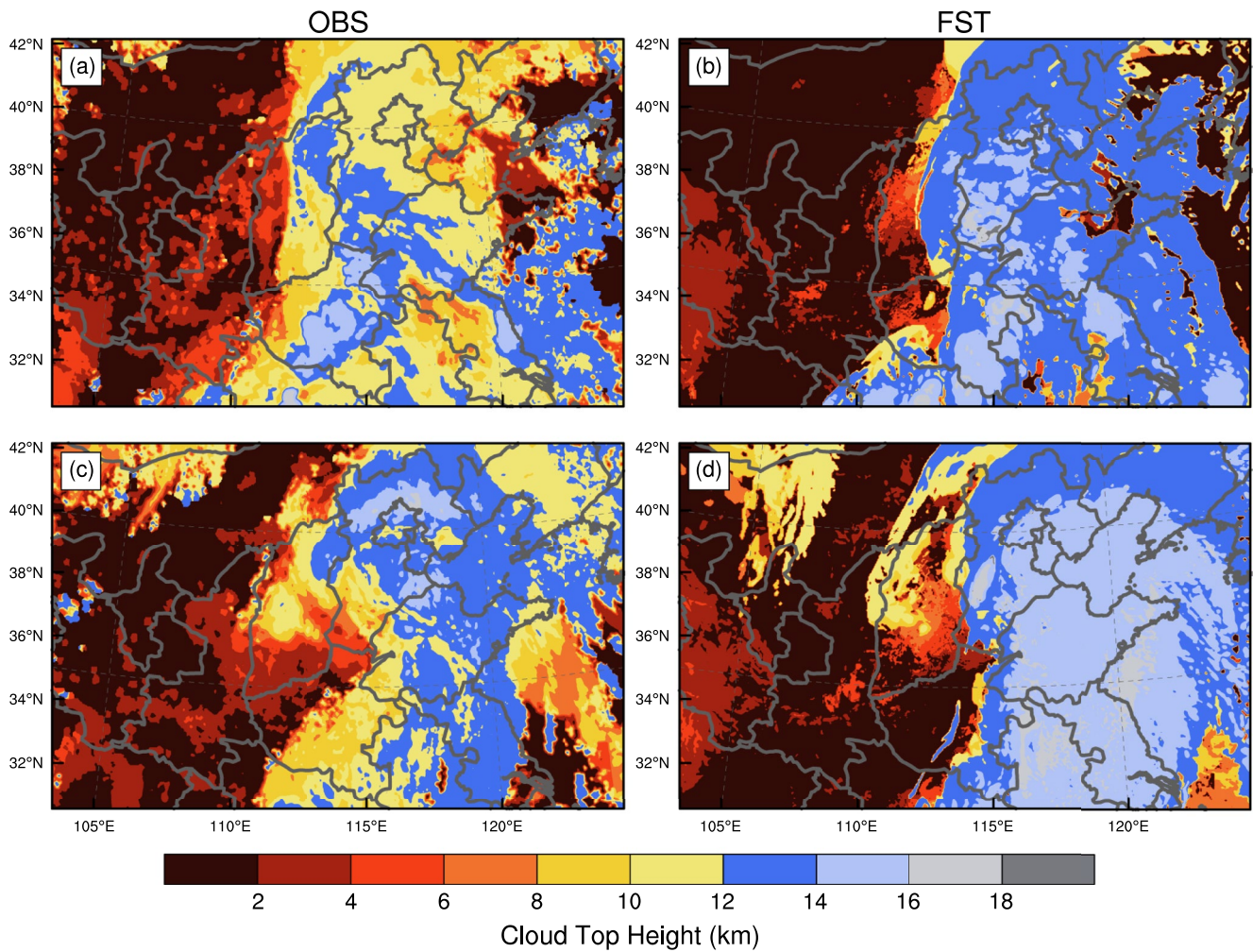


Figure 11. CTH of the (a, c) observation and (b, d) forecast at (a, b) 1200 UTC 19 July 2016 and (c, d) 0000 UTC 20 July 2016. The observed CTH comes from Himawari-8 AHI L2 class CTH products. The forecast CTH is derived from forecast profiles.

can be split into two parts: One is owing to the lapse rate and also the absorption and scattering effect within the over-predicted CTH, there is approximately -6.431 K per kilometer. The average lapse rate for the atmosphere is around -6.391 K near the cloud top, indicating the combined effect of absorption and scattering of cloud/hydrometeor particles is small. The other is from the temperature forecasting bias at the observed CTH.

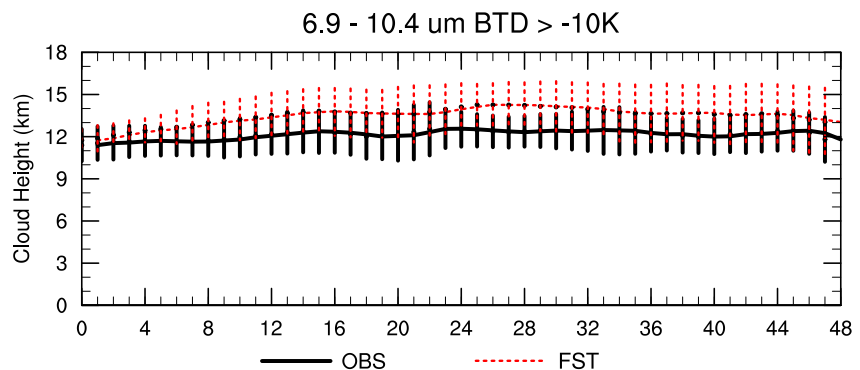


Figure 12. Time series of CTH for upper-level clouds (BTD > -10 K) during the forecast hours. The black solid line represents the mean value of observed CTH, and the error bars represent the standard error. The red dashed line and bars represent the forecast CTH mean value and standard error, respectively.

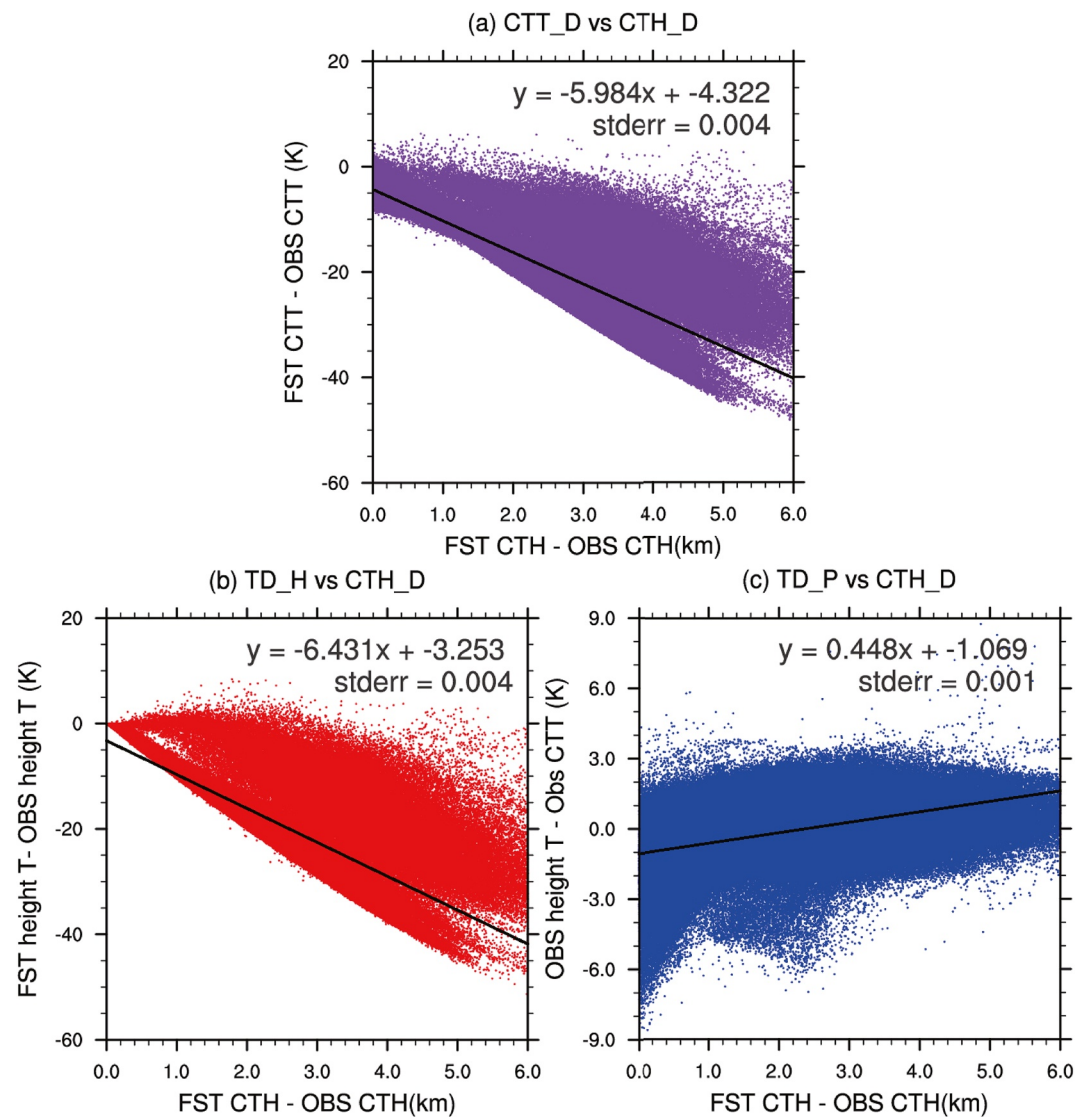


Figure 13. Scatterplots and lines of best fit for the (a) differences in CTT between the forecast and observation versus those of CTH, (b) differences in temperature at the forecast and observed CTH versus CTH errors, and (c) temperature of the observed CTH minus the observed CTT versus CTH errors at 0000 UTC 20 July 2016.

The result reveals a positive bias of about 0.448 K per kilometer (Figure 13c). This suggests that the predicted temperature biases have a small influence on the CTT simulation biases. Overall, better representativeness of cloud structure is key to a successful radiance simulation. The biases of simulated BT are highly sensitive to the biases of simulated CTH.

5.2. Sensitivity of Simulated BT to Hydrometeor Properties

In NWP models, the CTH is determined by the hydrometeor profiles of mixing ratios and number concentrations. To see which hydrometeor species has the largest impact on the accuracy of the simulated BT, a group of sensitivity experiments is conducted. Figure 14 illustrates the influence on the BT when removing one of the five hydrometeor species. Here, we use the mature stage at 0000 UTC 20 July as an example. Other times results in similar conclusions and are therefore not shown. The shape and simulated BT of the cloud field change dramatically without cloud ice (Figure 14d). This result is even more evident in the classification of dominant hydrometeor, which is defined as the hydrometeor whose removal results in the largest BT difference. Cloud ice dominates the simulated radiance for most of the cloudy region (Figure 14g). The removal of snow also has

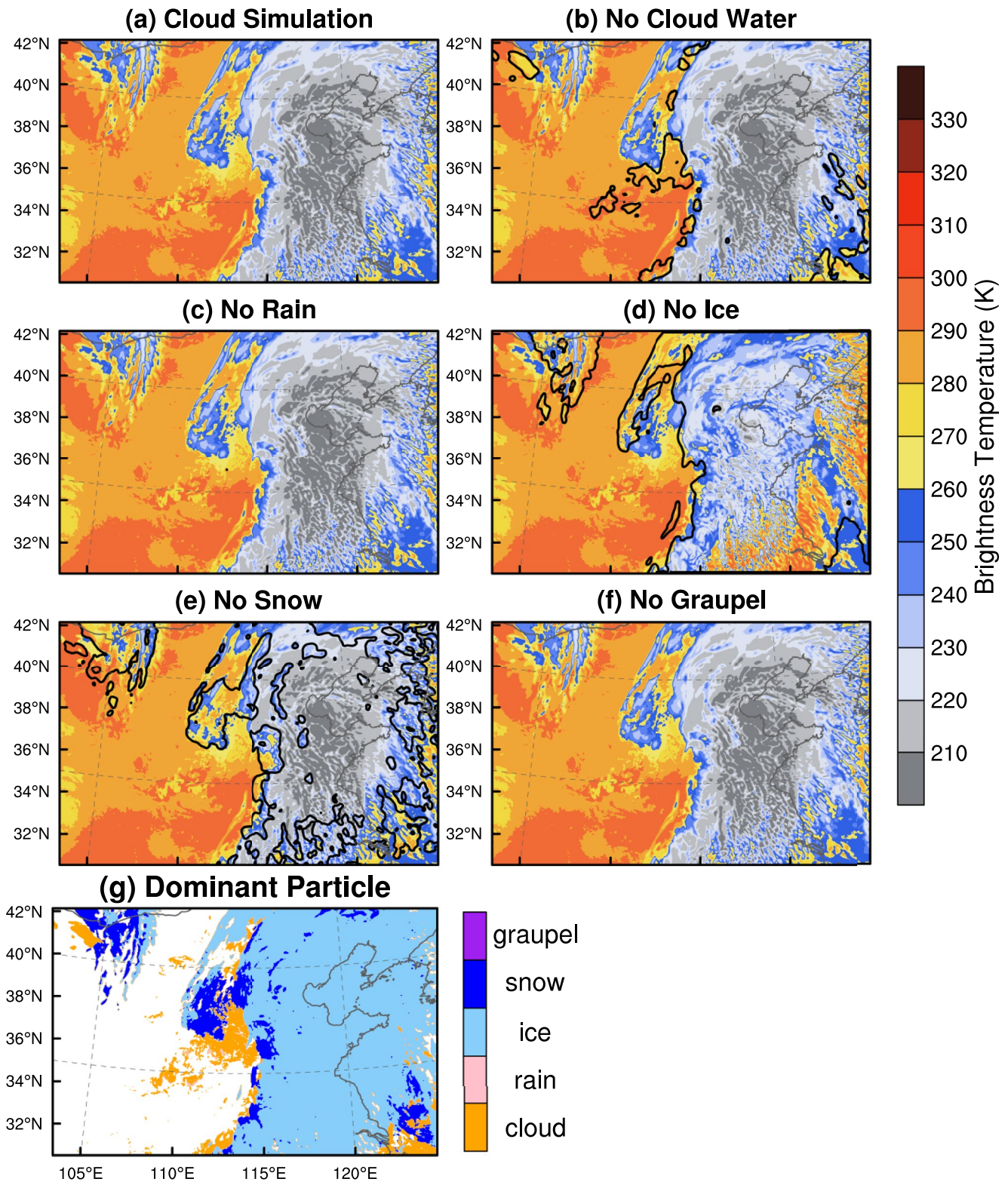


Figure 14. Simulated BT of the control experiment and sensitivity experiments involving the removal of specific cloud hydrometeor species at 0000 UTC 20 July 2016. The black line is 5K BT difference contour. A dominant particle is defined as that resulting in the largest BT difference when removed.

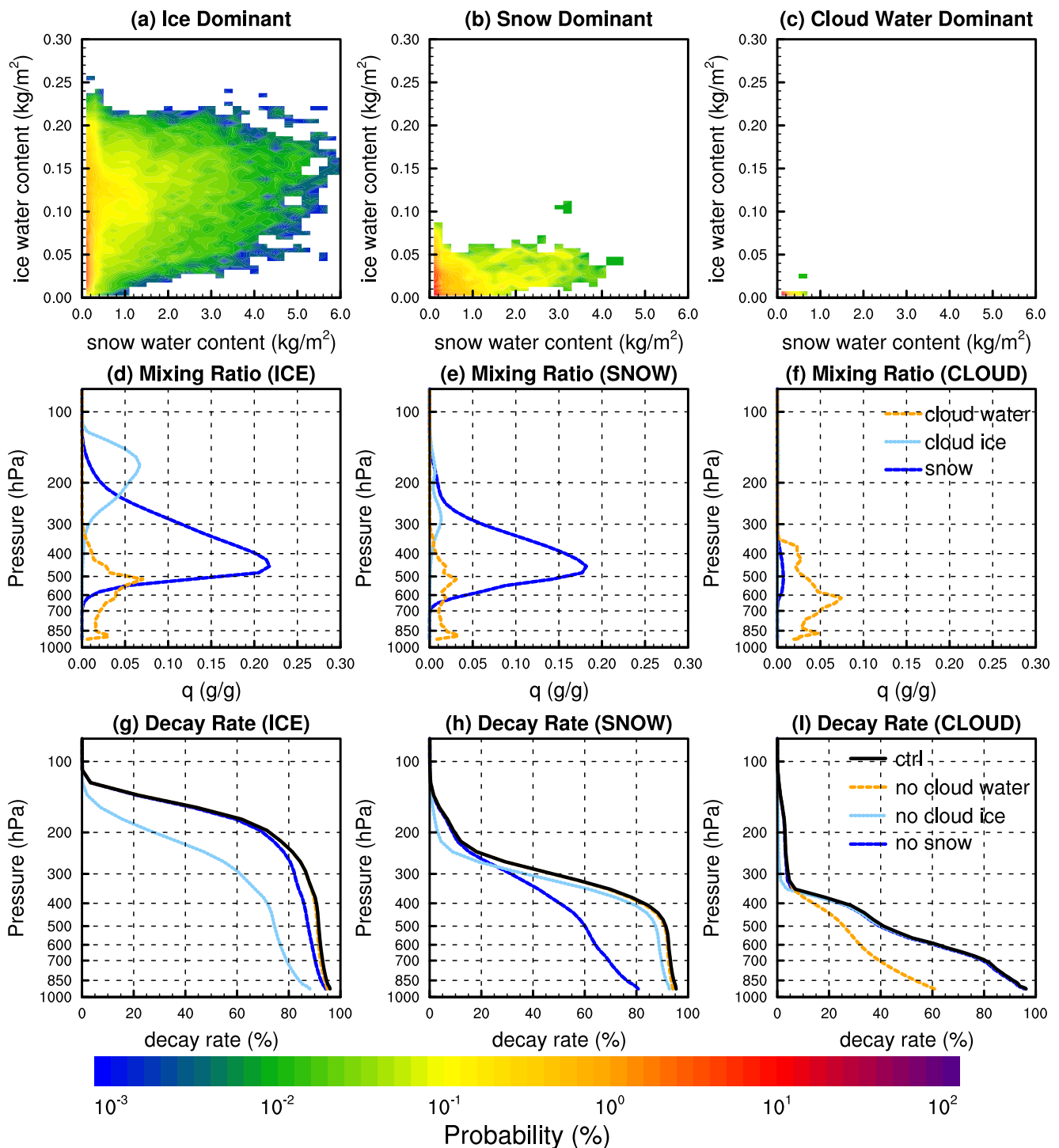


Figure 15. Probability distribution of (a) ice, (b) snow and (c) cloud water dominated region (see Figure 14g), and vertical profiles of mixing ratio, 10.4- μ m radiance decay rate of the (d, g) ice-, (e, h) snow-, and (f, i) cloud-water-dominated region at 0000 UTC 20 July 2016.

an impact in the cloud boundary regions where the cloud ice content is low (Figures 14e and 14g). Cloud water dominates the cloud region near the melting level (Figures 14b and 13g), and it can be seen that the differences with and without cloud water between 260 and 280 K (see yellow shaded area in Figure 14a) are obvious. For other hydrometeor variables, including rain and graupel, the impacts are barely visible. The purple (corresponding to graupel) and pink (corresponding to rain) colors are absent in Figure 14g.

Figure 15 illustrates why the comparable regions of simulated BT in Figure 14g is dominated by ice, snow, and cloud water, respectively. For the ice-dominated zone, there are two evident high-density centers. One of them corresponds to the deep convection area (see the ice content at about 0.125 kg m^{-2} and snow content at around 0.5 kg m^{-2}). The snow content is higher in that area; however, it peaks at about 450 hPa (see the blue line in Figure 15d). By comparison, the ice content peaks at roughly 170 hPa (see the cyan line in Figure 15d). Here, we use the rate of decay to explain why ice dominates the simulated radiance. The total transmittance is calculated using the transmittance profile (from the optical depth profile simulated by CRTM) integrated from the given level to the model top. It indicates how much of the radiation emitted from that layer can reach the satellite. The percentage of radiation cannot reach the satellite is referred to as the rate of decay. For this case, the average simulated CTH is at around 150 hPa, where the total transmittance decreases rapidly. The rate of decay reaches 0.9 at around 200 hPa, which explains well why the simulated radiance is mostly affected by the levels around the CTH. The levels below the CTH contribute limited outgoing radiance. Not surprisingly, the rate of decay is determined by ice, as the exclusion of ice results in the largest difference (see the cyan line in Figure 15g). The snow has a small impact below 150 hPa (see the blue line in Figure 15g); however, clearly, the contribution is not comparable to that of ice. The other dominated region corresponds to the cloud anvil, which is mostly filled by cloud ice (Twohy & Poellot, 2005). For that region, snow is extremely low (no more than 0.2 kg m^{-2}) and mostly below 200 hPa.

For the snow-dominated region, the total ice mixing ratio of most grid points is below 0.1 g kg^{-1} (Figure 15b). Vertically, the ice content is low above 200 hPa and comparable to that of snow. Although ice still dominates the variation in the rate of decay above 200 hPa, the overall rate of decay is only reduced to 30% (see the black line in Figure 15h)—significantly lower than that of the ice-dominated region at 90% (see the black line in Figure 15g). Snow becomes the dominant hydrometeor type when the ice content above 200 hPa is thin so as to have limited impact on the rate of decay. This explains the results of Griffin et al. (2020) that lower BTs of Thompson scheme are associated with larger snow content above 400 hPa rather than cloud ice at cloud top, because Thompson scheme tends to have very thin cloud ice near cloud top due to its strict limit on the cloud ice particle number concentration (0.25 cm^{-3} much lower than the 10 cm^{-3} of the Morrison). For the cloud-water-dominated region, there is thin ice and snow above the cloud water, but their contribution can be neglected. Overall, cloud ice dominates most of the region, followed by snow and cloud water. The simulated radiance is sensitive to the vertical distribution and content of hydrometeor species within the microphysics scheme. Accurate prediction of hydrometeor species is therefore also important to successful BT simulation.

5.3. Sensitivity of Simulated BT to Effective Radius

Another important property related to BT simulation, as discussed above, is the effective radii of hydrometeor species. In CRTM, the effective radius is used as an index of optical properties and is one of the key parameters. However, for simplicity, it is often assumed to be constant in various applications. Figure 16 shows the fixed and diagnosed effective radii using the formulation in Section 3.3. For the real atmosphere, the larger particles tend to fall faster than smaller ones. The size-sorting mechanism (van Dienenhoven et al., 2016) will result in smaller particles in the upper levels and larger particles at the lower levels. The fixed effective radii is clearly unrealistic for hydrometeor species (Kumjian & Ryzhkov, 2012). For the ice particles, the use of fixed radius of $50 \mu\text{m}$ is larger than the diagnosed one above approximately 150 hPa but smaller at levels below (Figure 16a). Similar results are seen for diagnosed effective radius of snow (Figure 16d). For cloud water, the fixed value of $20 \mu\text{m}$ is consistently larger than the diagnosed values (about $5 \mu\text{m}$, see Figure 16g). Note that the Morrison scheme uses a fixed number concentration for cloud water, which may lead to an unrealistic effective radius.

Figure 16 provides further results on how the diagnosed effective radii influence the optical properties of the clouds, three-dimensionally. In CRTM, for the $10.9\text{-}\mu\text{m}$ infrared band, Mie scattering is used, while the effective radius is used as an index of optical properties. For Mie scattering, the forward scattering lobe becomes stronger and narrower with increasing spherical diameter, and vice versa (Acharya, 2017). In the ice-particle-dominated region, the effective radius diagnosed by the two-moment scheme is smaller than the fixed value above 150 hPa (cloud top). Forward scattering is a little weaker but backward scattering becomes stronger as the particle scale decreases. More radiation is reflected to the satellite. Below 150 hPa, the diagnosed effective radius is larger, forward scattering becomes stronger, and more radiation from below can pass through. With the transmittance increasing, the satellite receives more radiation from relatively lower clouds, and hence improves the simulated radiance. For the snow-particle-dominated region, the diagnosed effective radius in the high-concentration region

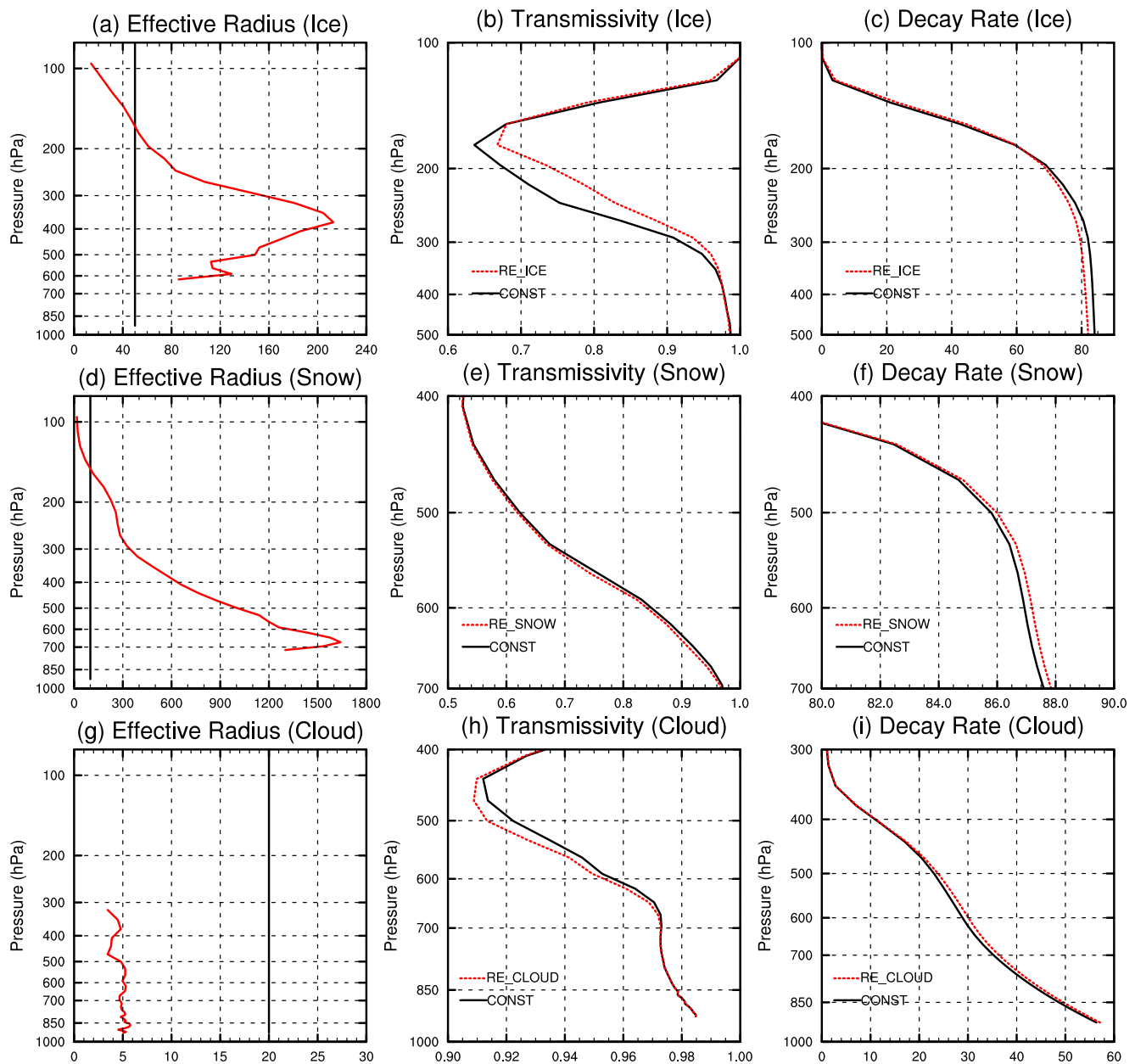


Figure 16. Vertical profiles of effective radius, layer transmissivity, and radiance decay rate for ice, snow and cloud water species at 0000 UTC 20 July 2016, averaged in their dominant regions (see Figure 14g). The black solid line represents results using the fixed effective radius in the ARPS model. The red dashed line represents the output using the effective radius diagnosed by the double-moment scheme.

is much higher than the given fixed radius of 100 μm for levels below 150 hPa (Figure 16, second row). However, for ice phase particles, little change can be seen in the CRTM scattering properties when the effective radius exceeded around 100 μm (Ding et al., 2011), which explains the almost zero difference in transmissivity between the fixed and diagnosed effective radii used in Figure 16. For cloud water, the transmissivity decreases as the calculated effective radius increases around 500 hPa. Overall, the calculated radii can reflect better the particle size distributions, leading to more accurate presentation of optical properties of clouds and hence better simulation of BT.

Figure 17 shows the root-mean square errors (RMSEs) and mean biases (MEs) calculated for the experiments using diagnosed and fixed effective radii. Here, we focus mainly on the upper levels where $\text{BTD} > -10$ K. In general, the improvements for the upper levels are small, with no more than 5% throughout the forecast period

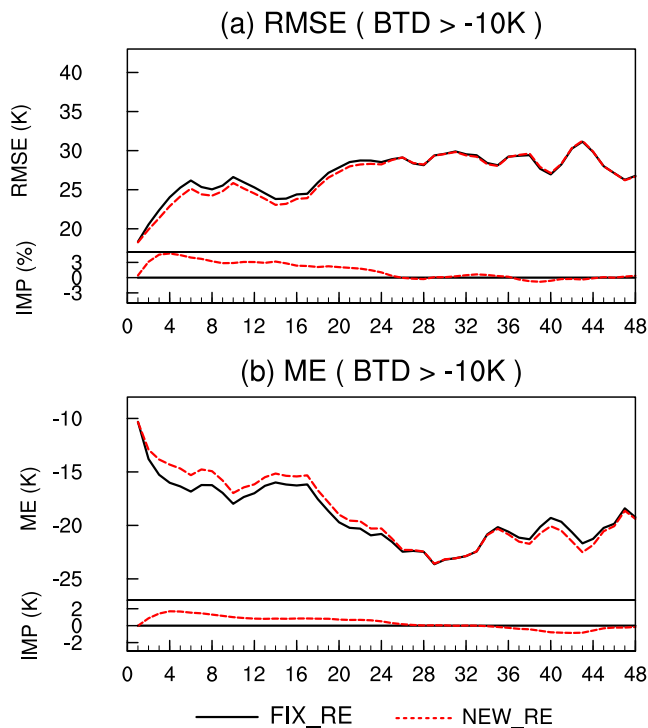


Figure 17. Time series of the (a) RMSE and (b) ME for upper-level clouds (BTD > -10 K). The black solid line and the red dashed line represent the value of the control experiment using fixed effective radius and the forecast using diagnosed effective radius, respectively.

in terms of RMSE. The ME is reduced, with a maximum of approximately 2 K. This is consistent with Shahabadi et al. (2016) who also pointed out that changes in optical properties in the radiative transfer model can affect individual optical profiles in the radiance simulations. Accuracy of effective radius, index of particle optical properties, is one of the error sources for BT simulation in the forward model, though their impacts are not as large as those caused by inaccurate cloud fields predicted by the NWP model. For this study, the improvement of using diagnosed effective radius is more obvious during the first day (Figure 17) than for the second. New convection continues to form along the east foot region of Taihang Mountains during the first 24 hr of forecast. The fixed effective radii, which are often based on those obtained from midlatitude and tropical field campaigns (Baum et al., 2011), may fail to reflect the average sizes of particles at the development stage of new convection, resulting in larger biases in simulated radiance. When the precipitation system becomes mature, there is still a significant difference in CTH, the fixed effective radius will not result in a significant difference from the diagnosed one. This is because the integrated transmissivity (rate of decay) between the fixed and diagnosed effective radii around the CTH is not significant (see in Figure 15c). Overall, the use of a diagnosed effective radius improves the BT simulation though the improvement tends to be small.

6. Summary and Conclusions

This paper evaluates the simulation of a LEC MCS that produced extreme rainfall over northern China from 19 to 21 July 2016 (maximum total accumulated rainfall of over 600 mm) using the WRF model at a 4-km convection-allowing resolution. The double-moment Morrison microphysics scheme is employed. The forecast of this extreme rainfall event is evaluated using gridded hourly precipitation, Himawari-8 geostationary satellite infrared BT, and radar reflectivity observations. The CRTM forward radiative transfer model is utilized to simulate the infrared BT that is compared to observations.

In general, the forecast reproduces the intensity, structure, and movement of precipitation system reasonably well. However, the simulated BT is lower than observed over most of the cloudy regions. Comparison with satellite observations shows that the CTH is over-predicted. Evaluation using the reflectivity observations shows that the heights of the convective cores of this LEC storm are also over-predicted, especially in the development stage. The model tends to develop cold and warm clouds above and below the freezing level simultaneously. The cold-cloud processes continue to intensify for the first few hours of forecast, resulting in deep convection during the development stage of the LEC storm. This is not consistent with radar observations, which indicate that warm processes dominate (Vitale & Ryan, 2013). For the mature stage, the over-prediction of the maximum height of the convective cores is reduced, but the cloud tops continue to be too high. This may have been due to the Morrison microphysics scheme tending to produce more cloud ice in the upper levels, resulting in higher CTH (Tiwari et al., 2018).

In addition, the sensitivity of the biases of the CRTM-simulated BT to cloud properties, including the CTH, cloud species and hydrometeor effective radii, is investigated. The bias in CTH simulation contributes most to the BT biases. For every kilometer of CTH over-prediction, there is a negative bias of about 6.4 K owing to the lapse rate and the extra cooling effect from the cloud particles near the cloud top. For most regions, cloud ice dominates the effects on simulated BT. Snow ranks second, but it mostly dominates very small areas of clouds where cloud ice is very low in quantity. Cloud water dominates the BT characteristics of low-level clouds near the main precipitation system. The impact of hydrometeor effective radii on the BT forecast bias is examined by replacing the radii calculated from particle size distributions predicted by the microphysics scheme by typically specified constant effective radii. In this study, the use of diagnosed radii makes a small improvement to the simulated BT during the first 24 hr of forecast. Overall, the predicted CTH is the most critical factor for successful simulation of BT,

which has important implications for the assimilation of BT observations in cloudy regions. The large error in the predicted CTH in this LEC case would pose significant problem when trying to directly assimilate the observed BT data into the model. The main sources of the problem deserve detailed investigations, and the treatments of microphysics processes for the specific thermodynamic environment may need much improvement.

In very recent years, the assimilation of cloud- and precipitation-affected radiances into NWP models have received increased attention, as the latest generation geostationary satellites are providing high spatial and temporal resolution observations that directly observe clouds and precipitation systems and regional operational models are running at convection-allowing resolutions (Li et al., 2021). The current study evaluates the performance of a convection-allowing model forecast for an extreme precipitation case that is characterized by low radar echo centroids and hence lower cloud tops, and tries to understand the main sources of biases in the simulated BT. Understanding of and efforts to reduce biases of simulated cloudy radiances, which serve as the background values of data assimilation, are important for their effective assimilation. Given that the simulated cloud properties, including CTH, are highly sensitive to the microphysics scheme, we plan to carry out sensitivity experiments using different microphysics schemes and perform similar investigations for more precipitation cases of China. Compared to LEC storms, deep convection dominated by both cold- and warm-cloud processes are more common over northern China. How well the model performs in the prediction of such convection will also be compared and evaluated. To better evaluate/verify forecasts within clouds, better observations such as those of polarimetric radars will be utilized in future work.

Data Availability Statement

All data sources used are freely available from the following website: (a) The precipitation observations can be obtained from the China Meteorological Administration (CMA) Meteorological Data Centre website (<http://data.cma.cn/>); (b) the NCEP $1^\circ \times 1^\circ$ FNL are available at NCAR's Research Data Archive website (<https://rda.ucar.edu/datasets/ds083.2>); (c) Himawari-8 infrared radiance observations, cloud products, and the WRF forecasts can be found at the public data repository Harvard Dataverse through the following link: <https://doi.org/10.7910/DVN/IPGRJV> (Nan et al., 2022).

References

- Acharya, R. (2017). Chapter 3 - Interaction of waves with medium. In R. Acharya (Ed.), *Satellite signal propagation, impairments and mitigation* (pp. 57–86). Academic Press. <https://doi.org/10.1016/b978-0-12-809732-8.00003-x>
- Bauer, P., Auligne, T., Bell, W., Geer, A., Guidard, V., Heilliette, S., et al. (2011). Satellite cloud and precipitation assimilation at operational NWP centres. *Quarterly Journal of the Royal Meteorological Society*, *137*(661), 1934–1951. <https://doi.org/10.1002/qj.905>
- Bauer, P., Ohring, G., Kummerow, C., & Auligne, T. (2011). Assimilating satellite observations of clouds and precipitation into Nwp models. *Bulletin of the American Meteorological Society*, *92*(6), Es25–Es28. <https://doi.org/10.1175/2011bams3182.1>
- Baum, B. A., Yang, P., Heymsfield, A. J., Schmitt, C. G., Xie, Y., Bansemmer, A., et al. (2011). Improvements in shortwave bulk scattering and absorption models for the remote sensing of ice clouds. *Journal of Applied Meteorology and Climatology*, *50*(5), 1037–1056. <https://doi.org/10.1175/2010jamec2608.1>
- Bennartz, R., & Greenwald, T. (2011). Current problems in scattering radiative transfer modelling for data assimilation. *Quarterly Journal of the Royal Meteorological Society*, *137*(661), 1952–1962. <https://doi.org/10.1002/qj.953>
- Bessho, K., Date, K., Hayashi, M., Ikeda, A., Imai, T., Inoue, H., et al. (2016). An introduction to Himawari-8/9-Japan's new-generation geostationary meteorological satellites. *Journal of the Meteorological Society of Japan*, *94*(2), 151–183. <https://doi.org/10.2151/jmsj.2016-009>
- Caracena, F., Maddox, R. A., Hoxit, L. R., & Chappell, C. F. (1979). Meso-analysis of the Big Thompson storm. *Monthly Weather Review*, *107*(1), 1–17. [https://doi.org/10.1175/1520-0493\(1979\)107<0001:motbts>2.0.co;2](https://doi.org/10.1175/1520-0493(1979)107<0001:motbts>2.0.co;2)
- Cintineo, R., Otkin, J. A., Xue, M., & Kong, F. Y. (2014). Evaluating the performance of planetary boundary layer and cloud microphysical parameterization schemes in convection-permitting ensemble forecasts using synthetic GOES-13 satellite observations. *Monthly Weather Review*, *142*(1), 163–182. <https://doi.org/10.1175/Mwr-D-13-00143.1>
- Collard, A. D., & McNally, A. P. (2009). The assimilation of infrared atmospheric sounding interferometer radiances at ECMWF. *Quarterly Journal of the Royal Meteorological Society*, *135*(641), 1044–1058. <https://doi.org/10.1002/qj.410>
- Collins, W. D., Rasch, P. J., Boville, B. A., Hack, J. J., McCaa, J. R., Williamson, D. L., et al. (2004). Description of the NCAR community atmosphere model (CAM 3.0). NCAR Tech. Note, TN-464+STR. 214 pp.
- Coniglio, M. C., Correia, J., Jr., Marsh, P. T., & Kong, F. (2013). Verification of convection-allowing WRF model forecasts of the planetary boundary layer using sounding observations. *Weather and Forecasting*, *28*(3), 842–862. <https://doi.org/10.1175/WAF-D-12-00103.1>
- Ding, S. G., Yang, P., Weng, F. Z., Liu, Q. H., Han, Y., van Deist, P., et al. (2011). Validation of the community radiative transfer model. *Journal of Quantitative Spectroscopy & Radiative Transfer*, *112*(6), 1050–1064. <https://doi.org/10.1016/j.jqsrt.2010.11.009>
- Dudhia, J. (1989). Numerical study of convection observed during the winter monsoon experiment using a mesoscale two-dimensional model. *Journal of the Atmospheric Sciences*, *46*(20), 3077–3107. [https://doi.org/10.1175/1520-0469\(1989\)046<3077:nsocod>2.0.co;2](https://doi.org/10.1175/1520-0469(1989)046<3077:nsocod>2.0.co;2)
- Fu, J. L., Ma, X. K., Chen, T., Zhang, F., Zhang, X. D., Sun, J., et al. (2017). Characteristics and synoptic mechanism of the July 2016 extreme precipitation event in North China. *Meteorological Monthly*, *43*, 528–539. <https://doi.org/10.7519/j.issn.1000-0526.2017.05.002>

Acknowledgments

This work was primarily supported by the National Key Research and Development Program of China (Grants 2018YFC1507303) and the National Natural Science Foundation of China (Grant Nos. 41730965, 41975124).

- Geer, A. J., Lonitz, K., Weston, P., Kazumori, M., Okamoto, K., Zhu, Y. Q., et al. (2018). All-sky satellite data assimilation at operational weather forecasting centres. *Quarterly Journal of the Royal Meteorological Society*, *144*(713), 1191–1217. <https://doi.org/10.1002/qj.3202>
- Griffin, S. M., Otkin, J. A., Nebuda, S. E., Jensen, T. L., Skinner, P. S., Gilleland, E., et al. (2021). Evaluating the impact of planetary boundary layer, land surface model, and microphysics parameterization schemes on cold cloud objects in simulated GOES-16 brightness temperatures. *Journal of Geophysical Research: Atmospheres*, *126*(15). <https://doi.org/10.1029/2021JD034709>
- Griffin, S. M., Otkin, J. A., Thompson, G., Frediani, M., Berner, J., & Kong, F. Y. (2020). Assessing the impact of stochastic perturbations in cloud microphysics using GOES-16 infrared brightness temperatures. *Monthly Weather Review*, *148*(8), 3111–3137. <https://doi.org/10.1175/Mwr-D-20-0078.1>
- Gustafsson, N., Janjic, T., Schraff, C., Leuenberger, D., Weissmann, M., Reich, H., et al. (2018). Survey of data assimilation methods for convective-scale numerical weather prediction at operational centres. *Quarterly Journal of the Royal Meteorological Society*, *144*(713), 1218–1256. <https://doi.org/10.1002/qj.3179>
- Han, Y., Delst, P. v., Liu, Q., Weng, F., Yan, B., Treadon, R., & Derber, J. (2006). JCSDACommunity RadiativeTransferModel (CRTM)—version 1. NOAA Tech. Report 122.
- Han, Y., van Delst, P., & Weng, F. Z. (2010). An improved fast radiative transfer model for special sensor microwave imager/sounder upper atmosphere sounding channels. *Journal of Geophysical Research: Atmospheres*, *115*. <https://doi.org/10.1029/2010jd013878>
- Hansen, J. E., & Travis, L. D. (1974). Light-scattering in planetary atmospheres. *Space Science Reviews*, *16*(4), 527–610. <https://doi.org/10.1007/Bf00168069>
- Honda, T., Miyoshi, T., Lien, G. Y., Nishizawa, S., Yoshida, R., Adachi, S. A., et al. (2018). Assimilating all-sky Himawari-8 satellite infrared radiances: A case of Typhoon Soudelor (2015). *Monthly Weather Review*, *146*(1), 213–229. <https://doi.org/10.1175/Mwr-D-16-0357.1>
- Huang, Y. J., Liu, Y. B., Liu, Y. W., & Knievel, J. C. (2019). Budget analyses of a record-breaking rainfall event in the coastal metropolitan city of Guangzhou, China. *Journal of Geophysical Research: Atmospheres*, *124*(16), 9391–9406. <https://doi.org/10.1029/2018jd030229>
- Jankov, I., Grasso, L. D., Sengupta, M., Neiman, P. J., Zupanski, D., Zupanski, M., et al. (2011). An evaluation of five ARW-WRF microphysics schemes using synthetic GOES imagery for an atmospheric river event affecting the California coast. *Journal of Hydrometeorology*, *12*(4), 618–633. <https://doi.org/10.1175/2010JHM1282.1>
- Jones, T. A., Skinner, P., Yussouf, N., Knopfmeier, K., Reinhart, A., Wang, X. G., et al. (2020). Assimilation of GOES-16 radiances and retrievals into the warn-on-forecast system. *Monthly Weather Review*, *148*(5), 1829–1859. <https://doi.org/10.1175/Mwr-D-19-0379.1>
- Karlsson, K. G. (1996). Validation of modelled cloudiness using satellite-estimated cloud climatologies. *Tellus A*, *48*(5), 767–785. <https://doi.org/10.3402/tellusa.v48i5.12206>
- Kumjian, M. R., & Ryzhkov, A. V. (2012). The impact of size sorting on the polarimetric radar variables. *Journal of the Atmospheric Sciences*, *69*(6), 2042–2060. <https://doi.org/10.1175/Jas-D-11-0125.1>
- Lai, R. Z., Teng, S. W., Yi, B. Q., Letu, H. S., Min, M., Tang, S. H., & Liu, C. (2019). Comparison of cloud properties from Himawari-8 and Fengyun-4A geostationary satellite radiometers with MODIS cloud retrievals. *Remote Sensing*, *11*(14), 1703. <https://doi.org/10.3390/rs11141703>
- Landel, G., Smith, J. A., Baeck, M. L., Steiner, M., & Ogden, F. L. (1999). Radar studies of heavy convective rainfall in mountainous terrain. *Journal of Geophysical Research: Atmospheres*, *104*(D24), 31451–31465. <https://doi.org/10.1029/1999jd900297>
- Li, J., Geer, A. J., Okamoto, K., Otkin, J. A., Liu, Z. Q., Han, W., & Wang, P. (2021). Satellite all-sky infrared radiance assimilation: Recent progress and future perspectives. *Advances in Atmospheric Sciences*, *39*, 9–21. <https://doi.org/10.1007/s00376-021-1088-9>
- Luo, L., Xiao, H., Yang, H. L., Chen, H. N., Guo, J., Sun, Y., & Feng, L. (2020). Raindrop size distribution and microphysical characteristics of a great rainstorm in 2016 in Beijing, China. *Atmospheric Research*, *239*, 104895. <https://doi.org/10.1016/j.atmosres.2020.104895>
- Maddox, R. A., Hoxit, L. R., Chappell, C. F., & Caracena, F. (1978). Comparison of meteorological aspects of Big Thompson and rapid city flash floods. *Monthly Weather Review*, *106*(3), 375–389. [https://doi.org/10.1175/1520-0493\(1978\)106<0375:comaot>2.0.co;2](https://doi.org/10.1175/1520-0493(1978)106<0375:comaot>2.0.co;2)
- Martin, G. M., Johnson, D. W., & Spice, A. (1994). The measurement and parameterization of effective radius of droplets in warm stratocumulus clouds. *Journal of the Atmospheric Sciences*, *51*(13), 1823–1842. [https://doi.org/10.1175/1520-0469\(1994\)051<1823:mapoe>2.0.co;2](https://doi.org/10.1175/1520-0469(1994)051<1823:mapoe>2.0.co;2)
- Mecikalski, J. R., & Bedka, K. M. (2006). Forecasting convective initiation by monitoring the evolution of moving cumulus in daytime GOES imagery. *Monthly Weather Review*, *134*(1), 49–78. <https://doi.org/10.1175/Mwr3062.1>
- Mecikalski, J. R., Mackenzie, W. M., Konig, M., & Muller, S. (2010). Cloud-top properties of growing cumulus prior to convective initiation as measured by Meteosat second generation. Part II: Use of visible reflectance. *Journal of Applied Meteorology and Climatology*, *49*(12), 2544–2558. <https://doi.org/10.1175/2010jame2480.1>
- Milbrandt, J. A., & Yau, M. K. (2005). A multimoment bulk microphysics parameterization. Part I: Analysis of the role of the spectral shape parameter. *Journal of the Atmospheric Sciences*, *62*(9), 3051–3064. <https://doi.org/10.1175/Jas3534.1>
- Min, M., Li, J., Wang, F., Liu, Z. J., & Menzel, W. P. (2020). Retrieval of cloud top properties from advanced geostationary satellite imager measurements based on machine learning algorithms. *Remote Sensing of Environment*, *239*, 111616. <https://doi.org/10.1016/j.rse.2019.111616>
- Min, M., Wu, C. Q., Li, C., Liu, H., Xu, N., Wu, X., et al. (2017). Developing the science product algorithm testbed for Chinese next-generation geostationary meteorological satellites: Fengyun-4 series. *Journal of Meteorological Research*, *31*(4), 708–719. <https://doi.org/10.1007/s13351-017-6161-z>
- Minamide, M., & Zhang, F. Q. (2018). Assimilation of all-sky infrared radiances from Himawari-8 and impacts of moisture and hydrometer initialization on convection-permitting tropical cyclone prediction. *Monthly Weather Review*, *146*(10), 3241–3258. <https://doi.org/10.1175/Mwr-D-17-0367.1>
- Morrison, H., Thompson, G., & Tatarskii, V. (2009). Impact of cloud microphysics on the development of trailing stratiform precipitation in a simulated squall line: Comparison of one- and two-moment schemes. *Monthly Weather Review*, *137*(3), 991–1007. <https://doi.org/10.1175/2008mwr2556.1>
- Nan, Y., Zhu, K., & Xue, M. (2022). Himawari-8 infrared observation, cloud products, and the WRF forecast of an extreme precipitation event in northern China on 19–21 July 2016 [Dataset]. Harvard Dataverse. <https://doi.org/10.7910/DVN/IPGRJV>
- Otkin, J. A. (2010). Clear and cloudy sky infrared brightness temperature assimilation using an ensemble Kalman filter. *Journal of Geophysical Research: Atmospheres*, *115*(19). <https://doi.org/10.1029/2009jd013759>
- Otkin, J. A., & Greenwald, T. J. (2008). Comparison of WRF model-simulated and MODIS-derived cloud data. *Monthly Weather Review*, *136*(6), 1957–1970. <https://doi.org/10.1175/2007mwr2293.1>
- Petersen, W. A., Carey, L. D., Rutledge, S. A., Knievel, J. C., Doesken, N. J., Johnson, R. H., et al. (1999). Mesoscale and radar observations of the Fort Collins flash flood of 28 July 1997. *Bulletin of the American Meteorological Society*, *80*(2), 191–216. [https://doi.org/10.1175/1520-0477\(1999\)080<0191:maroot>2.0.co;2](https://doi.org/10.1175/1520-0477(1999)080<0191:maroot>2.0.co;2)
- Pleim, J. E. (2007). A combined local and nonlocal closure model for the atmospheric boundary layer. Part I: Model description and testing. *Journal of Applied Meteorology and Climatology*, *46*(9), 1383–1395. <https://doi.org/10.1175/JAM2539.1>

- Pleim, J. E., & Xiu, A. J. (2003). Development of a land surface model. Part II: Data assimilation. *Journal of Applied Meteorology*, 42(12), 1811–1822. [https://doi.org/10.1175/1520-0450\(2003\)042<1811:doalsm>2.0.co;2](https://doi.org/10.1175/1520-0450(2003)042<1811:doalsm>2.0.co;2)
- Pontrelli, M. D., Bryan, G., & Fritsch, J. M. (1999). The Madison County, Virginia, flash flood of 27 June 1995. *Weather and Forecasting*, 14(3), 384–404. [https://doi.org/10.1175/1520-0434\(1999\)014<0384:tmcvff>2.0.co;2](https://doi.org/10.1175/1520-0434(1999)014<0384:tmcvff>2.0.co;2)
- Qin, Z. K., Zou, X. L., & Weng, F. Z. (2013). Evaluating added benefits of assimilating GOES imager radiance data in GSI for coastal QPFs. *Monthly Weather Review*, 141(1), 75–92. <https://doi.org/10.1175/Mwr-D-12-00079.1>
- Sawada, Y., Okamoto, K., Kunii, M., & Miyoshi, T. (2019). Assimilating every-10-minute Himawari-8 infrared radiances to improve convective predictability. *Journal of Geophysical Research: Atmospheres*, 124(5), 2546–2561. <https://doi.org/10.1029/2018jd029643>
- Shahabadi, M. B., Huang, Y., Garand, L., Heilliette, S., & Yang, P. (2016). Validation of a weather forecast model at radiance level against satellite observations allowing quantification of temperature, humidity, and cloud-related biases. *Journal of Advances in Modeling Earth Systems*, 8(3), 1453–1467. <https://doi.org/10.1002/2016ms000751>
- Shi, X. K., Li, Y. D., Liu, J. W., Xiang, X. Z., & Liu, L. (2018). Simulation of FY-2D infrared brightness temperature and sensitivity analysis to the errors of WRF simulated cloud variables. *Science China Earth Sciences*, 61(7), 957–972. <https://doi.org/10.1007/s11430-017-9150-0>
- Sieron, S. B., Clothiaux, E. E., Zhang, F. Q., Lu, Y. H., & Otkin, J. A. (2017). Comparison of using distribution-specific versus effective radius methods for hydrometeor single-scattering properties for all-sky microwave satellite radiance simulations with different microphysics parameterization schemes. *Journal of Geophysical Research: Atmospheres*, 122(13), 7027–7046. <https://doi.org/10.1002/2017jd026494>
- Sieron, S. B., Zhang, F. Q., Clothiaux, E. E., Zhang, L. N., & Lu, Y. H. (2018). Representing precipitation ice species with both spherical and nonspherical particles for radiative transfer modeling of microphysics-consistent cloud microwave scattering properties. *Journal of Advances in Modeling Earth Systems*, 10(4), 1011–1028. <https://doi.org/10.1002/2017ms001226>
- Skamarock, W. C. (2004). Evaluating mesoscale NWP models using kinetic energy spectra. *Monthly Weather Review*, 132(12), 3019–3032. <https://doi.org/10.1175/Mwr2830.1>
- Skamarock, W. C., Klemp, J. B., Dudhia, J., Gill, D. O., Barker, D., Duda, M. G., et al. (2008). A description of the advanced Research WRF version 3. NCAR Tech. Note, NCAR/TN-475+STR. 113 <https://doi.org/10.5065/D68S4MVH>
- Smith, J. A., Baeck, M. L., Steiner, M., & Miller, A. J. (1996). Catastrophic rainfall from an upslope thunderstorm in the central Appalachians: The Rapidan storm of June 27, 1995. *Water Resources Research*, 32(10), 3099–3113. <https://doi.org/10.1029/96wr02107>
- Thompson, G., & Eidhammer, T. (2014). A study of aerosol impacts on clouds and precipitation development in a large winter cyclone. *Journal of the Atmospheric Sciences*, 71(10), 3636–3658. <https://doi.org/10.1175/Jas-D-13-0305.1>
- Thompson, G., Field, P. R., Rasmussen, R. M., & Hall, W. D. (2008). Explicit forecasts of winter precipitation using an improved bulk microphysics scheme. Part II: Implementation of a new snow parameterization. *Monthly Weather Review*, 136(12), 5095–5115. <https://doi.org/10.1175/2008mwr2387.1>
- Thompson, G., Tewari, M., Ikeda, K., Tessoroff, S., Weeks, C., Otkin, J., & Kong, F. Y. (2016). Explicitly-coupled cloud physics and radiation parameterizations and subsequent evaluation in WRF high-resolution convective forecasts. *Atmospheric Research*, 168, 92–104. <https://doi.org/10.1016/j.atmosres.2015.09.005>
- Tiwari, S., Kar, S. C., & Bhatla, R. (2018). Dynamic downscaling over Western Himalayas: Impact of cloud microphysics schemes. *Atmospheric Research*, 201, 1–16. <https://doi.org/10.1016/j.atmosres.2017.10.007>
- Twohy, C. H., & Poellot, M. R. (2005). Chemical characteristics of ice residual nuclei in anvil cirrus clouds: Evidence for homogeneous and heterogeneous ice formation. *Atmospheric Chemistry and Physics*, 5, 2289–2297. <https://doi.org/10.5194/acp-5-2289-2005>
- van Diedenhoven, B., Fridlind, A. M., Cairns, B., Ackerman, A. S., & Yorks, J. E. (2016). Vertical variation of ice particle size in convective cloud tops. *Geophysical Research Letters*, 43(9), 4586–4593. <https://doi.org/10.1002/2016gl068548>
- Vitale, J., & Ryan, T. (2013). Operational recognition of high precipitation efficiency and low-echo-centroid convection. *Journal of Operational Meteorology*, 1(12), 128–143. <https://doi.org/10.15191/nwajom.2013.0112>
- Weng, F. Z. (2007). Advances in radiative transfer modeling in support of satellite data assimilation. *Journal of the Atmospheric Sciences*, 64(11), 3799–3807. <https://doi.org/10.1175/2007jas2112.1>
- Xie, B., Fung, J. C. H., Chan, A., & Lau, A. (2012). Evaluation of nonlocal and local planetary boundary layer schemes in the WRF model. *Journal of Geophysical Research: Atmospheres*, 117. <https://doi.org/10.1029/2011jd017080>
- Zhang, Y. J., Zhang, F. Q., & Stensrud, D. J. (2018). Assimilating all-sky infrared radiances from GOES-16 ABI using an ensemble Kalman filter for convection-allowing severe thunderstorms prediction. *Monthly Weather Review*, 146(10), 3363–3381. <https://doi.org/10.1175/Mwr-D-18-0062.1>
- Zhao, S., Sun, J., Lu, R., & Fu, S. (2018). Analysis of the 20 July 2016 unusual heavy rainfall in north China and Beijing. *Meteorological Monthly*, 44, 351–360.
- Zhong, L. Z., Mu, R., Zhang, D. L., Zhao, P., Zhang, Z. Q., & Wang, N. (2015). An observational analysis of warm-sector rainfall characteristics associated with the 21 July 2012 Beijing extreme rainfall event. *Journal of Geophysical Research: Atmospheres*, 120(8), 3274–3291. <https://doi.org/10.1002/2014jd022686>
- Zhu, K. F., & Xue, M. (2016). Evaluation of WRF-based convection-permitting multi-physics ensemble forecasts over China for an extreme rainfall event on 21 July 2012 in Beijing. *Advances in Atmospheric Sciences*, 33(11), 1240–1258. <https://doi.org/10.1007/s00376-016-6202-z>
- Zhu, K. F., Xue, M., Zhou, B. W., Zhao, K., Sun, Z. Q., Fu, P. L., et al. (2018). Evaluation of real-time convection-permitting precipitation forecasts in China during the 2013–2014 summer season. *Journal of Geophysical Research: Atmospheres*, 123(2), 1037–1064. <https://doi.org/10.1002/2017jd027445>
- Zou, X. L., & Da, C. (2014). An objective regional cloud mask algorithm for GOES infrared imager radiance assimilation. *Journal of Geophysical Research: Atmospheres*, 119(11), 6666–6680. <https://doi.org/10.1002/2014jd021455>
- Zou, X. L., Qin, Z. K., & Weng, F. Z. (2011). Improved coastal precipitation forecasts with direct assimilation of GOES-11/12 imager radiances. *Monthly Weather Review*, 139(12), 3711–3729. <https://doi.org/10.1175/Mwr-D-10-05040.1>